Austrian Journal of Earth Sciences | Vienna | 2026 | Volume 119 | 1–19 | DOI: 10.17738/ajes.2026.0001

Old orogen – young topography: Linking rift evolution, thermal overprinting, and apatite (U-Th)/He thermochronology in the Black Forest and Vosges Mountains

Fabian Dremel[1], Nicolas Villamizar-Escalante[1], Bianca Heberer[1], Bjarne Friedrichs[1], Lea Schönleber[1], Jörg Robl[1], Christoph von Hagke[1]

[1)] Department of Environment and Biodiversity, University Salzburg, 5020 Salzburg, Austria

[*)] Corresponding author: Fabian Dremel, fabian.dremel@plus.ac.at

Keywords: Low-temperature thermochronology, continental rifting, Upper Rhine Graben

Abstract

Investigating the thermal evolution of continental rifts is essential for understanding how lithospheric extension, surface uplift, and exhumation are recorded in the shallow crust. However, interpreting low-temperature thermochronological data in rift settings remains challenging, particularly where exhumation magnitudes are small and geothermal gradients are elevated and spatially heterogeneous. In such environments, cooling ages may reflect a combination of regional tectonic processes and localized thermal overprints, complicating the reconstruction of rift-related exhumation histories. Here, we present new apatite (U-Th)/He ages from the Black Forest and Vosges Mountains, integrated with published apatite fission-track data, to reconstruct the Cenozoic thermal evolution of the Upper Rhine Graben rift flanks. Sampling along multiple transects perpendicular to the rift axis provides the spatial resolution required to distinguish regional cooling trends from localized thermal perturbations. The data and time-temperature modeling indicate that maximum temperatures were reached during the Late Cretaceous to Paleocene, approaching but generally not exceeding the apatite partial retention and annealing zones (PRZ/PAZ). Cooling occurred in three main phases during the Late Cretaceous, Eocene, and Oligocene, resulting in pronounced single-grain apatite (U-Th)/He age dispersion. A regionally pervasive Miocene reheating event is not required to explain the observed age patterns. Instead, the data are best explained by a combination of incomplete resetting, radiation damage effects, and localized hydrothermal influences in the vicinity of normal faults. These results highlight the importance of integrating multiple low-temperature thermochronometers with high spatial sampling density to disentangle tectonically driven cooling from localized thermal overprinting in intracontinental rift systems.

1. Introduction

Investigating the thermal and tectonic evolution of continental rifts is essential for understanding how lithospheric deformation translates into long-term exhumation, surface uplift, and landscape evolution (Bosworth, 1985; Brune et al., 2023; Dremel et al., 2025; Kettermann et al., 2019; Neuharth et al., 2022; Rosendahl, 1987). Low-temperature thermochronology has become a key tool in this context, as it enables reconstruction of cooling and exhumation histories over million-year time scales and provides direct constraints on the interaction between tectonics and the shallow crust (Ehlers and Farley, 2003; Flowers et al., 2022a; Link, 2009; Timar-Geng et al., 2006). However, applying thermochronological methods in continental rift settings remains challenging, particularly where exhumation magnitudes are small and

geothermal gradients vary strongly in space and time (Dremel et al., 2025; Flowers et al., 2022a; Green and Duddy, 2018).

These limitations are especially pronounced along rift shoulders, where landscape evolution models predict only minor amounts of exhumation, often close to or below the detection limits of commonly used thermochronometers (Bishop, 2007; Dremel et al., 2025), such as apatite fission-track or apatite (U-Th)/He dating with closure temperatures below ~120°C and ~90°C, respectively (Flowers et al., 2022b and references therein). In such settings, thermochronological ages may be influenced not only by regional-scale tectonic processes, but also by localized thermal perturbations associated with fault-controlled fluid flow or transient changes in the geothermal gradient (Frings et al., 2025; Lupi et al., 2010; Saspiturry et al., 2020). As a result, disentangling tectonically driven cooling from thermally induced overprinting remains a central challenge in interpreting low-temperature thermochronological data from continental rifts (Boone et al., 2021).

Previous studies have demonstrated the potential of thermochronology to constrain rift evolution, particularly using apatite fission-track data to derive first-order exhumation histories (Su et al., 2021; Timar-Geng et al., 2006; Turab et al., 2023). Conceptual and numerical models linking normal faulting, exhumation, and thermochronological signals have provided a framework for understanding how fault-controlled deformation shapes cooling paths in extensional settings (Ehlers and Farley, 2003; Ketcham, 2005; Stüwe et al., 1994; Mancktelow and Grasemann, 1997). Nevertheless, many studies rely on single thermochronometers or limited spatial sampling, restricting their ability to resolve thermal histories and to assess the relative contributions of regional exhumation versus localized thermal effects (e.g., Dresmann et al., 2010; Timar-Geng et al., 2006; Mansour et al., 2025; Rohrman et al., 1994). This is particularly problematic in rifts characterized by elevated and heterogeneous geothermal gradients (Brune et al., 2023; Lysak, 1992; Schellschmidt and Clauser, 1996; Starostenko et al., 1999).

Within this context, the Upper Rhine Graben represents a natural laboratory for testing thermochronological interpretations in intracontinental rift systems (Fig. 1). The rift is characterized by ongoing tectonic activity, exceptionally high geothermal gradients, and well-documented structural inheritance, yet it has experienced only modest amounts of Cenozoic exhumation (Dresmann et al., 2010; Schellschmidt and Clauser, 1996; Schumacher, 2002; Timar-Geng et al., 2006). Accordingly, fission-track approaches may be insufficiently sensitive to fully resolve the Miocene to recent thermal history of the rift shoulders, whereas an approach including apatite (U-Th)/He dating with its lower closure temperature has greater potential to resolve this phase.

Here we present a new high-resolution (U-Th)/He thermochronological data set from both flanks of the Upper Rhine Graben, complementing previous studies, that predominantly reported fission track data (Dresmann, 2009; Link, 2009; Timar-Geng, 2006). Combined with new thermal modeling, this data allows us to refine our understanding of cooling mechanisms, and, in turn, the temporal evolution of exhumation associated with continental rifting.

2. Geological setting

The Upper Rhine Graben is located within the Variscan belt, a Late Paleozoic orogen whose structures still influence the region's tectonics today (Kroner and Romer, 2013; Matte, 2001, 1986). Following Variscan orogenesis, prolonged erosion and post-orogenic extension led to the development of a Permian peneplain, subsequently overlain by up to ~1500 m of Triassic to Jurassic sedimentary sequences deposited during phases of subsidence and marine transgression (Dresmann et al., 2010; Geyer and Gwinner, 1991; Häring, 2002; Timar-Geng, 2006).

During the Cretaceous and Paleocene, domal uplift of the Rhenish Shield (~130 Ma) and collision-related intraplate thrusting (~80 Ma) resulted in a phase of non-deposition and erosion within Central Europe (Barbarand et al., 2018; Kley and Voigt, 2008; Olivetti et al., 2020; Ziegler and Dèzes, 2007). Hydrothermal activity and vein mineralization during this period (~130 Ma and ~90 Ma) have been related to extensional settings due to the opening of the Atlantic (Ziegler, 1992; Wetzel et al., 2003). As a response to increasing compressional stresses from the Alpine orogeny, the URG formed as a passive rift in the northern alpine foreland (Ziegler, 1990; Illies, 1972). During the late Eocene, subsidence of the URG commenced with isolated depressions that further connected to large basins along pre-existing Variscan fault systems (Schumacher, 2002; Ziegler, 1990; Ziegler et al., 2004; Hinsken et al., 2007).

A tectonic transition occurred during the Miocene, when lithospheric folding associated with the Alpine orogeny temporarily reversed the long-term subsidence of the southern and central URG, leading to transient uplift of the graben floor (Ziegler and Dèzes, 2007). This phase, expressed by rapid uplift of the southern rift flanks, persisted until the Pliocene (Dèzes et al., 2004). The deposition and deformation of Pliocene-Quaternary sediments subsequently indicate a renewed phase of subsidence in the southern URG (Giamboni et al., 2004b, 2004a; Dèzes et al., 2004). Although several viable mechanisms have been proposed to explain this uplift, including lithospheric-scale folding, lower-crustal flow, and far-field Alpine compressional stresses, the relative importance of these processes and their timing remain poorly constrained (Dèzes et al., 2004; Schumacher, 2002).

Structurally, the URG is bounded by subparallel sets of normal faults, most prominently the Eastern and Western Main Border Faults (EMBF and WMBF), which separate the graben from the Black Forest and Vosges Mountains, respectively (e.g., Grimmer et al., 2017). Displacements

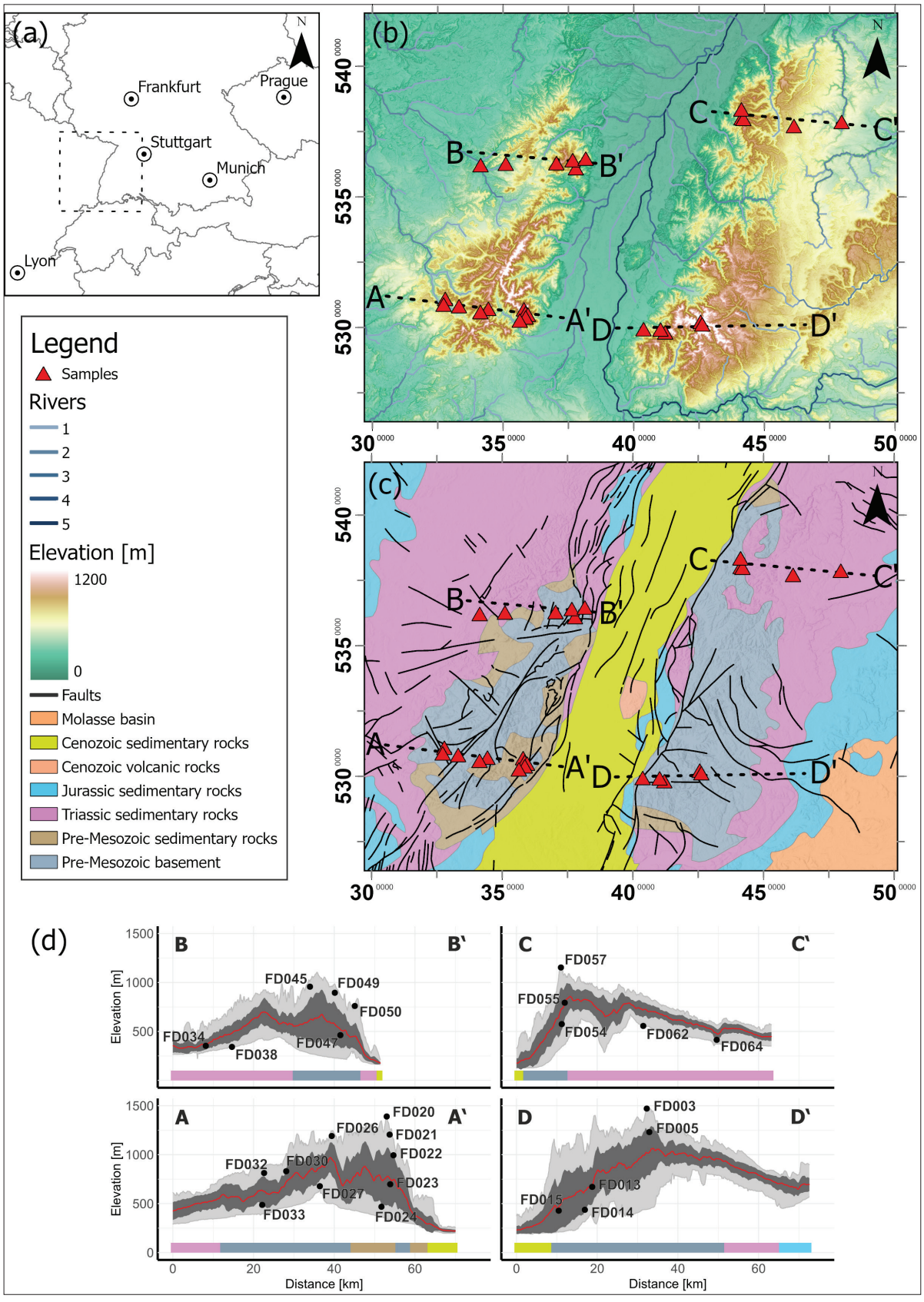

Figure 1: (a) Location of the study area within Central Europe. **(b)** Topographic map of the study area with location of samples and swath profiles. River networks are color-coded according to the Strahler order. **(c)** Chronostratigraphic map based on Asch (2003, IGME 5000, BGR) with sample locations, swath profiles and dominant fault zones (v. Gessel et al., 2021). **(d)** Swath profiles with a swath width of 10 km. Location of swath profiles is marked as dashed lines in (b) and (c). Profiles are shown as mean (red line), 1σ (dark grey), and minimum/maximum (light grey). Samples are labeled and shown regarding elevation and distance along the profiles. Colored bar at the bottom depicts chronostratigraphy from (c).

along these fault systems reach several kilometers and control rift architecture and exhumation patterns (Rotstein et al., 2006; Rotstein and Schaming, 2008; Grimmer et al., 2017).

Nowadays, the URG forms the largest segment of the northern European Cenozoic Rift System and extends approximately 300 km from Basel in the south to Frankfurt in the north (Fig. 1c). Recent geodetic and seismic data indicate that continental rifting within the URG remains tectonically active, with subsidence rates of up to 0.5 mm a^{-1}. The southern Vosges Mountains and Black Forest are marked by uplift rates of up to 1 mm a^{-1} contrasting with subsidence of up to 2 mm a^{-1} for their northern counterparts (Fuhrmann et al., 2013; Serpelloni et al., 2013; Sternai et al., 2019; Piña-Valdés et al., 2022). Collectively, these observations demonstrate ongoing tectonic and thermal activity within the URG. In contrast, the timing, magnitude, and spatial configuration of exhumation along its flanks remain poorly constrained and are therefore the focus of this study.

3. Methodology

3.1. Apatite (U-Th)/He thermochronology

Apatite (U-Th)/He thermochronology is based on thermally activated diffusion of radiogenic helium in the crystal lattice. Upon crystallization, ^{147}Sm, ^{232}Th, ^{235}U, and ^{238}U are incorporated at ppm levels into the crystal lattice. Due to varying travel distances of the emitted α-particles (^{4}He atoms), these can be either ejected from or retained within the crystal. In moderately damaged apatite, temperature sensitivity of the crystals ranges between 67 and 69 °C for an assumed cooling rate of 10 °C Ma^{-1} (Flowers et al., 2022b). Radiation damage, caused by the recoil of α-particles during the decay of U and Th and their α-emitting daughter nuclides, introduces defects into the crystal lattice. These defects increase helium retentivity, which can shift the effective closure temperature to approximately 40–115 °C (Flowers et al., 2022b; Shuster et al., 2004). Annealing of these defects occurs at temperatures comparable to those of fission-track annealing (Gautheron et al., 2009; Shuster et al., 2006; Flowers et al., 2009).

To adequately account for the parent-nuclide, dependent stopping distances of α-particles within apatite crystals, (U-Th)/He ages require correction procedures that incorporate both grain size and the intra-crystalline distribution of U and Th (Flowers et al., 2022b; Ketcham et al., 2011; Cooperdock et al., 2019). For further information, the reader is referred to Flowers et al. (2022b), Flowers et al. (2022a), Farley (2002), and Ehlers and Farley (2003).

3.2. Thermochronological data

In total, we collected 40 new samples from the Vosges Mountains and the Black Forest for apatite (U-Th)/He thermochronology, of which 26 yielded apatite in sufficient quantity and quality for analysis (Fig. 2). Sampling targeted both vertical elevation profiles and horizontal transects across rift shoulders and fault-bounded basement blocks. The southern profiles follow previously investigated transects using apatite fission-track dating in the southern Vosges Mountains and Black Forest (Timar-Geng et al. 2006), as well as new east-west profiles across the northern Vosges Mountains and Black Forest (Fig. 1b, d; Tab. 1). Samples were collected mainly from Variscan crystalline basement, granitoids and gneisses, to ensure lithological comparability across profiles (Fig. 1c; Tab. 1) (lithological description according to the geological maps 1:50 000 of France (BRGM, 2025) and Germany (Regierungspräsidium Freiburg, 2021) is listed in Tab. 1). Two samples were taken from outcropping (meta-)sediments, including Visean greywacke and Triassic sandstone. At outcrops containing both crystalline basement and intrusive rocks, bulk samples were collected, as the intrusive lithologies are of Variscan age and thus share a similar pre-rift thermal history as the host rocks (e.g., FD014, FD032 and FD049). New AHe data are complemented by a compilation of published apatite fission-track and apatite (U-Th)/He single-grain ages (99 AFT and 43 AHe ages) from the study area (Dresmann, 2009; Link, 2009; Timar-Geng, 2006).

3.3. Analytical procedure

Samples were processed following standard apatite (U-Th)/He preparation and analytical procedures. After crushing, milling, and sieving, apatite crystals were separated using a combination of density and magnetic techniques. Suitable grains were hand-picked under cross-polarized light based on established selection criteria (Farley, 2002; Flowers et al., 2022b; Reiners, 2005), measured, photographed, and packed into Pt capsules. Helium was extracted by laser heating and analyzed by isotope dilution using a quadrupole mass spectrometer. U, Th, and Sm concentrations were determined by quadrupole ICP-MS following complete grain dissolution and external calibration. Measurements of two to five replicates were performed on 26 out of 40 samples, as these yielded apatite crystals of sufficient amount, size, and quality. Alpha-ejection corrections were applied following Ketcham et al. (2011) and Cooperdock et al. (2019). The total uncertainty of the dates takes both TAU and additional FT correction uncertainties (typically 5 %) into account. A detailed description of the analytical procedures is provided in Supplement S1, and analytical results are reported in Supplements S2 and S3.

Replicates of MK-1 (Wu et al., 2019) and Durango (McDowell et al., 2005) reference apatite were degassed, dissolved and analyzed. In total, 19 measurements were conducted on MK-1 (10 measurements) and Durango (9 measurements) apatite (Tab. 2). These standard measurements are consistent with the intercalibrated dates of MK-1 (18.00 ± 0.2 Ma) (Wu et al., 2021) and Durango (31.02 ± 1.01 Ma) (McDowell et al., 2005; Wu et al., 2019) (see Supplements S4 and S5 for analytical results).

Table 1: Weighted-mean age, standard error of the weighted-mean, and mean square of weighted deviates for apatite standards MK-1 and Durango. For a full description of the formulas and further information, the reader is referred to Flowers et al. (2022a).

	$SE_{W,IU}$ [Ma]	$MSWD_W$	Replicas	Dispersion [%]
MK-1	17.98 ± 0.01	0.1	10	0.6
Durango	32.43 ± 0.78	2.6	9	2.5

Table 2: Apatite (U-Th)/He sample information. Coordinates are given in WGS84 (EPSG-Code: 4326). Rock type is taken from the geological maps 1:50 000 of France (BRGM, 2025) and Germany (Regierungspräsidium Freiburg, 2021) with the respective map sheet listed in a separate column. Stratigraphic age is derived from (Asch, 2003, IGME 5000, BGR).

Name	Lat [°]	Lon [°]	Z [m]	Map sheet	Rock type	(Stratigraphic) age
FD003	47.87208	8.0045	1471	DE8710	Migmatite with paragneiss relics	Paleozoic
FD005	47.86334	8.01309	1231	DE8710	Migmatite with paragneiss relics	Paleozoic
FD013	47.83401	7.8246	671	DE8710	Marginal granite (Randgranit)	Paleozoic
FD014	47.84353	7.80008	437	DE8710	Migmatite with paragneiss relics	Paleozoic
FD015	47.84366	7.71348	428	DE8710	Paragneiss and anatectically overprinted gneisses	Paleozoic
FD020	47.90369	7.09938	1390	FR068	Greywacke	Visean
FD021	47.89059	7.10828	1205	FR068	Porphyritic granite	Visean – Namurian
FD022	47.88519	7.12054	994	FR068	Porphyritic granite	Visean – Namurian
FD023	47.87573	7.10926	698	FR068	Porphyritic granite	Visean – Namurian
FD024	47.86452	7.07952	468	FR068	Porphyritic granite	Lower Visean
FD026	47.90228	6.91711	1191	FR088	Late- to post-orogenic dikes composed of quartz-bearing microgranite	Namurian
FD027	47.8905	6.87698	678	FR088	Late- to post-orogenic dikes composed of quartz-bearing microgranite	Namurian
FD030	47.9083	6.76675	831	FR088	Porphyroid granite	Tournaisian – Visean
FD032	47.932	6.69496	813	FR088	Calc-alkaline porphyroid granite	Tournaisian – Visean
FD033	47.91242	6.68747	487	FR088	Calc-alkaline porphyroid granite	Namurian
FD034	48.39593	6.85701	307	FR088	Calc-alkaline leucogranite	Stephanian
FD038	48.40303	6.98719	342	FR088	Pyroclastic rocks	Middle Devonian
FD045	48.40913	7.2486	957	FR067	biotite granite	Namurian (319 ± 3 Ma)
FD047	48.39347	7.34966	462	FR067	biotite–amphibole granodiorite	Upper Visean (329 ± 2 Ma)
FD049	48.42093	7.33231	895	FR067	heterogeneous amphibole-bearing diorites	Upper Visean (331 Ma)
FD050	48.4272	7.39953	760	FR067	heterogeneous amphibole-bearing diorites	Upper Visean (331 Ma)
FD054	48.57513	8.20323	575	DE7910	Seebach granite	Pennsylvanian
FD055	48.57248	8.21299	793	DE7910	Seebach granite	Pennsylvanian
FD057	48.60483	8.20211	1153	DE7910	Forbach granite	Pennsylvanian
FD062	48.54942	8.47527	556	DE7910	Forbach granite	Pennsylvanian
FD064	48.56433	8.72279	414	DE7918	Plattensandstone Formation	Anisian

3.4. Thermal modeling

To reconstruct the post-Jurassic thermal evolution, we performed inverse thermal history modeling using QTQt (Gallagher, 2012). Individual samples containing more than one dated apatite crystal (n > 1) were modeled separately to assess sample-specific thermal histories. Samples collected along the vertical profile at the Grand Ballon (FD021, FD022, FD023, FD024) were modeled jointly as a single elevation profile spanning ~730 m and were combined with published AFT data from nearby samples (ZTG101, ZTG102, and ZTG103; Timar-Geng et al., 2006). For the AFT data, only single-grain ages (spontaneous and induced track counts for 20 grains per sample) were used. Track-length data were not included because the etching protocol applied in the original study (1.1M HNO_3 for 40 seconds, Timar-Geng et al. (2006)) differs from the etching conditions implemented in QTQt and cannot be consistently parameterized within the software. Radiation damage effects on apatite (U-Th)/He ages were accounted for using the radiation damage accumulation and annealing model (RDAAM) by Gautheron et al. (2009). This model was selected because most samples display a positive age-eU relationship and no significant correlation between age and crystal size.

In total, three thermal constraints were applied to represent the known thermal history, including basement crystallization and subsequent burial-related reheating. The initial constraint represents Variscan crystallization of the basement rocks (330 ± 20 Ma, 820 ± 80 °C) (e.g., Schaltegger, 2000; Zeh et al., 2024). To account for sediment deposition and burial-related heating, we applied a second constraint during the Triassic (225 ± 25 Ma, 10 ± 10 °C) (Miller and Baranyi, 2021) and a third constraint during the Jurassic (175 ± 25 Ma, 50 ± 15 °C), reflecting the accumulation of approximately 1–1.5 km of sediments during these periods (Häring, 2002; Dresmann et al., 2010). While QTQt permits the use of time-variable geothermal gradients, we did not allow gradient variations in our models. Instead, a constant geothermal gradient of 45 °C km^{-1} (Dresmann et al., 2010; Schellschmidt and Clauser, 1996) was imposed to facilitate conversion of modeled cooling into theoretical exhumation, based on independently constrained sediment thicknesses. Jurassic excess temperatures were therefore calculated based on the maximum sediment thickness and the imposed geothermal gradient. In addition, a present-day surface temperature of 10 ± 10 °C was assumed. A full model setup following the recommendations by Abbey et al. (2023) is reported in the supplement S6.

4. Results

4.1. Apatite (U-Th)/He data

In total, 113 single-grain measurements from 26 samples yielded cooling ages ranging from 10.3 ± 0.6 (FD033_a02) to 179.5 ± 11.7 Ma (FD020_a05) (Fig. 2, Tab. 3, Supplementary data S2 and S3). Replicates that have been excluded from further interpretation due to (a) high deviations between calculated mass from grain size measurements and stoichiometric mass balance, (b) TAU > 10 %, (c) cracked crystals, or (d) age outlier that might reflect inherited He are marked based on these criteria in Table 3. For samples exhibiting a dispersion of ≤ 20 %, weighted-mean ages and weighted standard deviations were calculated to provide representative cooling ages (Flowers et al., 2022a). This threshold was chosen to minimize the influence of age variability arising from radiation damage, differences in crystal size, effective uranium (eU) zonation, grain fragmentation, helium implantation, inclusions, inherited helium, or other factors (Flowers et al. 2022a). In contrast, samples with high dispersion, especially those from the southern Black Forest, exhibited mean values exceeding 40 % and replicates have been treated as single-grain cooling ages.

A generally positive correlation between age and elevation is observed along all profiles, with older cooling ages typically associated with higher elevations (Figs. 3, 4). However, individual crystals reveal cooling ages that deviate from the other replicates of a sample, with substantially younger (e.g., FD003_a03 and FD033_a02) or older ages (e.g., FD020_a05 and FD032_a01), resulting in a deviation from this elevation-dependent age distribution (Figs. 3, 4a). Sampled vertical profiles include the rift flanks of the southern Vosges Mountains (FD020–FD024) (A–A′ in Fig. 1d), the northern Vosges Mountains (FD047–FD050) (B–B′ in Fig. 1d), and the northern Black Forest (FD054–FD057) (C–C′ in Fig. 1d). Both profiles from the Vosges Mountains display a clear age-elevation relationship (Figs. 3, 4a), with lower-elevated samples yielding maximum single-grain ages of ~54 Ma in the southern profile and ~41 Ma in the northern profile (FD047), whereas higher elevations record substantially older ages of up to ~180 Ma (FD020) and ~68 Ma (FD049 and FD050), respectively. In contrast, the northern Black Forest profile shows no systematic increase in cooling ages with elevation.

An additional pattern emerges when considering horizontal sample distribution: ages tend to increase at similar elevations with increasing distance from the Upper Rhine Graben (Figs. 2, 4c, 5). This general trend is less obvious for samples along profiles B and C, where the westernmost and easternmost samples reveal the youngest cooling ages along the profiles (Samples FD034 and FD064, respectively). These samples yielded the youngest weighted-mean ages of 33.4 ± 0.8 and 27.3 ± 0.7 Ma, i.e., younger than the general trend would suggest.

4.2. Thermal models

Model reliability was assessed based on the visual fit between predicted and observed single-grain ages. While QTQt reports nearly identical acceptance "birth & death" values for all models (Supplement S6), inspection of predicted versus observed ages reveals that several models reproduce the data only poorly (Supplement S7). Consequently, these models are considered of limited ro-

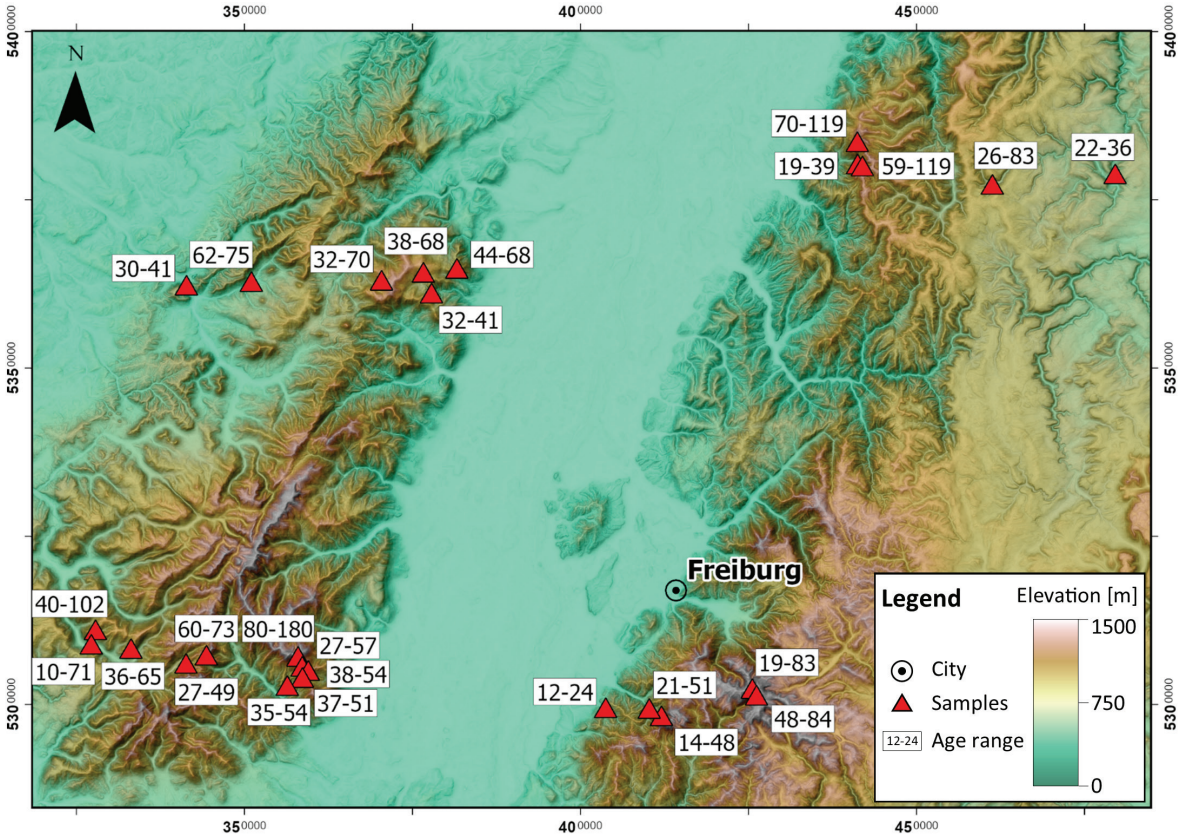

Figure 2: Topographic map showing single-grain age ranges for 26 samples that yielded apatite in sufficient quantity and quality for (U-Th)/He analysis. Red triangles mark sample locations; white boxes show minimum and maximum cooling ages in Ma for every sample.

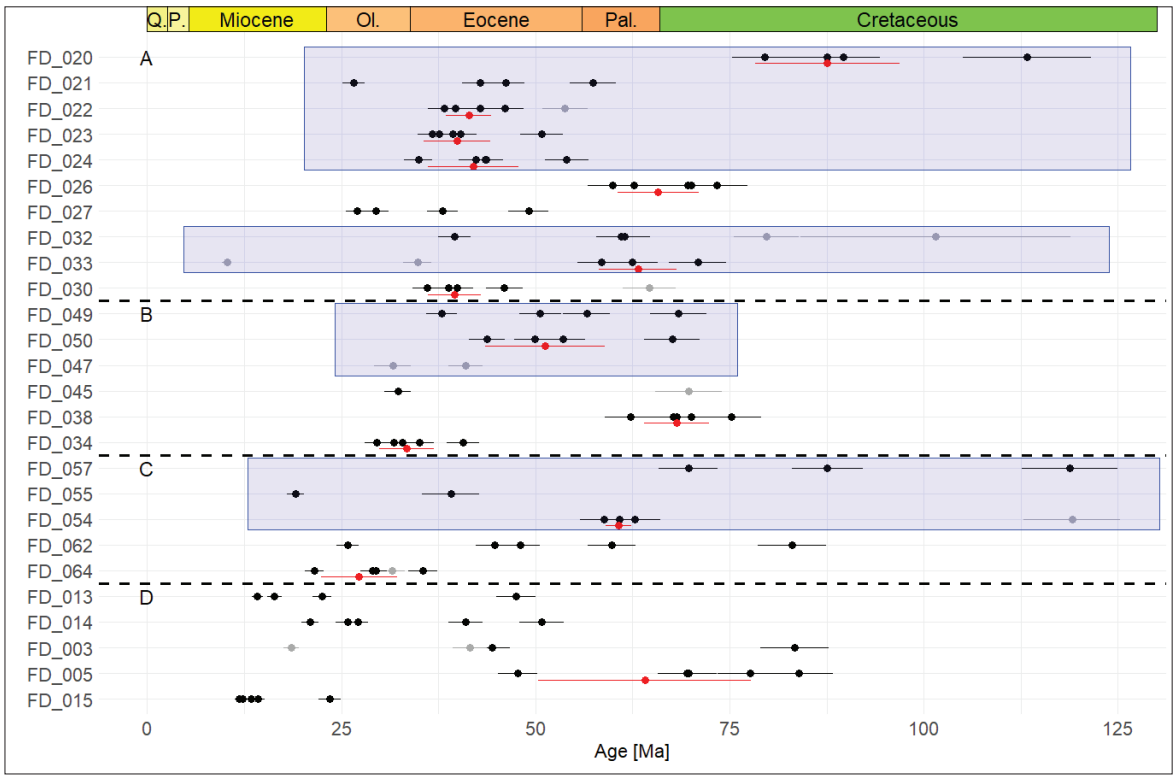

Figure 3: Distribution of measured single-grain ages with error bars. Letters A–D correspond to sections of swath profiles (Fig. 1). Ages in gray have been excluded from further interpretation (see Tab. 3 for further information). Red points represent calculated weighted-mean ages with error bars for samples with a dispersion ≤ 20 %. Blue boxes highlight consistent age-elevation profiles, with elevation increasing from bottom to top within the respective boxes.

Table 3: Relevant results from Apatite (U-Th)/He analyses. Full table is given in the Supplement S2 & S3. Samples excluded for further analysis are annotated with either **(a)** top and bottom 5 % of ratio between calculated mass from grain size measurements and stoichiometric mass balance, **(b)** TAU > 10 %, **(c)** cracked crystals, **(d)** age outlier that might reflect inherited He. TAU stands for total analytical uncertainty, FT for alpha ejection correction, TAU + FT includes total analytical uncertainty and alpha ejection correction. Calculated mean age resembles weighted-mean age (Flowers et al., 2022a).

Name	^{4}He [nmol/g]	U [ppm]	Th [ppm]	Sm [ppm]	Uncorr. date [Ma]	± TAU [Ma]	Corr. date [Ma]	± TAU + F_T [Ma]	Mean Age ± 1σ [Ma]
FD003_a01 (a)	3.2	16.76	3.47	54	33.6	0.5	41.6	2.2	
FD003_a02	5.69	14.78	6.81	55	63.8	1.2	83.4	4.4	
FD003_a03 (a)	0.8	9.22	2.38	36	15	0.3	18.6	1	
FD003_a05	3.75	17.86	5.76	63	36	0.6	44.4	2.3	
FD005_a01	49.31	174.4	0.81	312	52.1	0.8	77.6	4.1	
FD005_a02	10.24	57.43	1.92	211	32.6	0.6	47.7	2.5	
FD005_a03	58.25	222.1	6.47	360	48.1	0.8	69.7	3.7	64.1 ± 1.5
FD005_a04	36.09	108.3	1.36	285	61.2	1	83.9	4.4	
FD005_a05	52.79	191.19	10.71	379	50.3	0.8	69.5	3.7	
FD013_a01	2.82	54.1	3.53	290	9.5	0.2	14.2	0.7	
FD013_a02	6.42	78.62	9.84	262	14.7	0.2	22.5	1.2	
FD013_a03	11.71	59.66	11.2	266	34.6	0.6	47.5	2.5	
FD013_a04	5.86	87.52	21.63	296	11.7	0.2	16.4	0.9	
FD013_a05	8.71	52	2.8	276	30.5	0.6	47.5	2.5	
FD014_a01	2.13	22.36	7.56	47	16.4	0.5	25.8	1.5	
FD014_a02	4.53	23.61	3.74	28	34.2	0.9	50.8	2.9	
FD014_a03	4.15	39.34	3.77	48	19.1	0.4	27.1	1.4	
FD014_a04	2.08	26.74	0.6	54	14.4	0.3	21	1.1	
FD014_a05	6.5	45.25	5.57	86	25.8	0.6	41	2.2	
FD015_a01	0.99	19.13	6.82	70	8.8	0.2	12.3	0.7	
FD015_a02	0.86	14.65	2.71	55	10.4	0.2	13.4	0.7	
FD015_a03	0.46	8.43	3.44	55	9.1	0.2	11.9	0.6	
FD015_a04	0.59	10.09	1.49	47	10.5	0.3	14.3	0.8	
FD015_a05	1.02	11.6	0.97	52	16	0.6	23.5	1.4	
FD020_a01	2.33	3.99	4.47	285	79.7	4.3	113.3	8.3	
FD020_a02	14.35	26.3	83.38	142	57.4	1.1	89.6	4.8	87.6 ± 2.5
FD020_a03	15.22	25.48	80.79	174	62.7	1	79.5	4.2	
FD020_a04	4.3	8.09	20.06	285	60.3	1.6	87.6	5	
FD020_a05 (c, d)	6.44	6.71	10.28	378	123.5	5.2	179.5	11.7	
FD021_a01	7.05	38.63	30.3	531	28.1	0.6	42.9	2.3	
FD021_a03	7.75	63.56	65.58	610	18	0.3	26.6	1.4	
FD021_a04	8.66	38.83	47.01	539	31.7	0.5	46.2	2.4	
FD021_a05	9.63	31.46	38.75	385	43.3	0.7	57.4	3	
FD022_a01	10.44	61.6	33.06	524	27.6	0.4	39.7	2.1	
FD022_a02 (a)	9.01	42.41	27.31	456	33.8	0.6	53.8	2.9	
FD022_a03	14.98	64.16	53.41	541	35.8	0.6	46.1	2.4	43.0 ± 1.1
FD022_a04	11.58	59.68	25.11	500	32.4	0.5	42.9	2.3	
FD022_a05	7.63	46.26	33.76	495	25.8	0.5	38.3	2.1	
FD023_a01	5.6	29.68	26.12	462	28.5	0.5	40.3	2.1	
FD023_a02	7.04	34.55	40.33	545	29.1	0.4	36.7	1.9	
FD023_a03	9.93	50.67	54.8	540	28.6	0.5	39.3	2.1	39.9 ± 0.9
FD023_a04	7.11	40.92	31.37	439	27	0.4	37.6	2	
FD023_a05	23.49	108.13	9.8	317	39.2	0.6	50.8	2.7	
FD024_a01	11.46	44.32	62.34	461	35.6	0.6	42.3	2.2	
FD024_a02	7.15	40.93	52.37	466	24.6	0.4	34.9	1.8	
FD024_a03	13.26	52.39	71.61	545	35.1	0.5	43.6	2.3	42.0 ± 1.0
FD024_a04	8.37	34.45	41.18	396	34.7	0.6	43.5	2.3	
FD024_a05	8.12	28	25.82	387	43.4	0.7	54	2.8	
FD026_a01	7.43	23.24	42.62	336	40.7	0.9	70	7.2	
FD026_a03	11.42	31.05	50.29	307	48.7	0.8	69.6	3.7	
FD026_a06	12.14	30.41	54.52	321	51.4	0.8	73.4	3.9	65.8 ± 1.7
FD026_a07	11.22	28.86	46.67	291	51.5	0.8	62.7	3.3	
FD026_a08	9.02	30.43	44.04	283	40.5	0.7	59.9	3.2	

Name	^{4}He [nmol/g]	U [ppm]	Th [ppm]	Sm [ppm]	Uncorr. date [Ma]	± TAU [Ma]	Corr. date [Ma]	± TAU + F_T [Ma]	Mean Age ± 1σ [Ma]
FD027_a01	4.09	28.86	37.73	450	19.8	0.4	29.5	1.6	
FD027_a03	11.85	41.27	86.16	239	35.4	0.6	49.1	2.6	
FD027_a04	4.92	24.01	38.25	369	27.2	0.5	38	2	
FD027_a05	3.32	27.37	31.21	326	17.5	0.3	27	1.4	
FD030_a01	8.38	38.81	51.4	350	30.2	0.5	39.9	2.1	
FD030_a02 (c)	10.67	32.91	17.35	219	52.9	0.8	64.7	3.4	
FD030_a03	12.39	62.49	59.08	477	29.8	0.5	38.8	2	39.6 ± 1.0
FD030_a04	9.95	41.92	50.67	178	34	0.5	46	2.4	
FD030_a05 (a)	9.6	54.12	55.79	413	26.2	0.4	36.1	1.9	
FD032_a01 (b)	1.87	4.06	5.86	191	60.9	8.5	101.5	17.4	
FD032_a02	7.38	40.02	47.58	561	26.3	0.4	39.6	2.1	
FD032_a03 (a)	29.59	92.23	32.21	406	54.5	1	79.7	4.2	
FD032_a04	27.38	121.11	43.52	527	38.4	0.6	61	3.2	
FD032_a05	10.81	43.64	20.05	397	41	0.8	61.5	3.3	
FD033_a01	46.19	171.93	73.28	600	45	0.7	70.9	3.7	
FD033_a02 (a)	8.14	168.53	100.55	455	7.8	0.2	10.3	0.6	
FD033_a03	8.6	31.15	24.19	242	42.8	0.8	62.5	3.3	63.2 ± 1.9
FD033_a04	23.84	110.23	32.43	495	37.2	0.6	58.5	3.1	
FD033_a05 (a)	8.33	59.16	35.79	326	22.7	0.4	34.8	1.8	
FD034_a01	6.21	49.04	37.65	247	19.8	0.3	29.6	1.6	
FD034_a02	7.57	53.13	41.96	262	22.1	0.4	32.9	1.7	
FD034_a03	8.27	46.06	42.66	273	27.1	0.5	40.7	2.1	33.4 ± 0.8
FD034_a04	10.04	59.95	40.98	296	26.6	0.4	35.1	1.8	
FD034_a05	6.33	35.07	41.73	279	25.9	0.4	31.8	1.7	
FD038_a01	9.53	14.68	78.55	632	51.8	0.8	70.1	3.7	
FD038_a02	8.93	15.62	70.9	619	49.8	0.8	62.2	3.3	
FD038_a03	10.45	16.57	90.65	636	49.8	0.8	68.2	3.6	68.2 ± 1.6
FD038_a04	10.3	14.81	75.08	558	57.2	0.9	75.2	3.9	
FD038_a05	10.02	16.09	74.95	627	53.6	0.8	67.7	3.5	
FD045_a01	5.76	44.55	36.2	244	20	0.4	32.3	1.7	
FD045_a02 (c)	1.96	3.67	13.48	156	51.4	1.9	69.7	4.3	
FD047_a03 (a)	2.05	12.54	11.83	245	24.3	1.4	31.6	2.4	
FD047_a04 (a)	3.21	15.54	25.54	325	27.1	0.5	41	2.2	
FD049_a01	5.66	12.27	32.08	174	52.1	0.9	68.4	3.6	
FD049_a02	5.82	15.61	34.54	195	44.8	0.7	56.6	3	
FD049_a03	2.9	12.29	23.02	180	29.9	0.5	37.9	2	
FD049_a04	14.89	64.26	40.44	338	37.1	0.6	50.6	2.7	
FD050_a01	5.15	18.95	34.93	142	34.8	0.6	49.9	2.6	
FD050_a02	4.64	14.93	25.31	144	40.7	0.7	53.6	2.8	51.2 ± 1.4
FD050_a03	3.54	9.16	16.97	125	49.2	0.9	67.6	3.6	
FD050_a04	7.22	30.16	48.03	157	32.1	0.5	43.8	2.3	
FD054_a01	16.61	61.5	5.24	257	48.7	0.8	58.8	3.1	
FD054_a02	35.62	128.04	0.78	215	51.3	0.8	62.8	3.3	60.7 ± 1.8
FD054_a03	18.6	68.22	7.53	266	48.9	0.8	60.8	3.2	
FD054_a04 (d)	45.78	81.53	4.81	249	101.6	1.6	119.1	6.2	
FD055_a01	0.33	0.65	4.72	199	29.9	2.4	39.1	3.7	
FD055_a02	0.66	0.49	37.15	179	12.8	0.4	19.1	1.1	
FD057_a01	17.23	19.58	55.12	222	96.5	1.5	118.8	6.2	
FD057_a02	13.69	25.04	44.59	152	70.6	1.1	87.6	4.6	
FD057_a03	3.96	8.07	27.54	234	49.2	1.1	69.7	3.8	
FD062_a01	24.26	235.52	23.81	308	18.6	0.3	25.8	1.4	
FD062_a02	33.78	109.32	14.65	291	55.2	0.9	83	4.4	
FD062_a03	19.4	86.3	2.62	325	41.1	0.7	59.8	3.1	
FD062_a04	18.27	98.06	4.67	321	34	0.5	48.1	2.5	
FD062_a05	14.22	89.19	5.72	295	29	0.5	44.7	2.4	
FD064_a01	6.24	42.11	28.48	274	23.5	0.4	29.4	1.5	
FD064_a02	9.41	59.12	15.11	319	27.7	0.4	35.5	1.9	
FD064_a03	2.9	19.81	13.1	183	23.3	0.4	29	1.5	27.3 ± 0.7
FD064_a04 (a)	4.65	29.8	9.15	229	26.7	0.4	31.5	1.7	
FD064_a05	0.95	7.23	11.73	169	17.2	0.3	21.5	1.2	

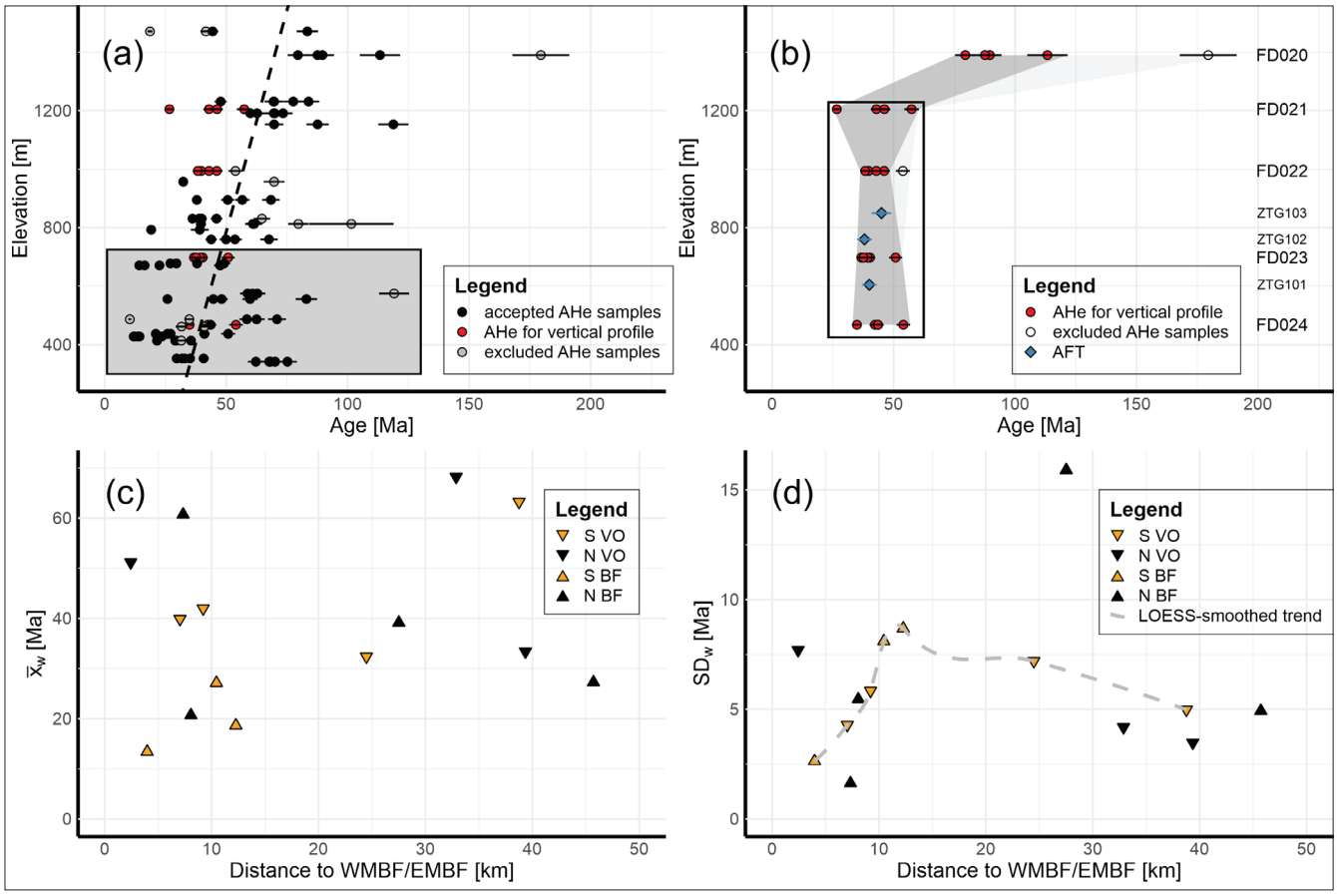

Figure 4: (a) Age-elevation plot for new AHe samples with error bars. Black points depict samples that were accepted for interpretation, grey points were excluded (see Tab. 3). Red points represent samples that were used for a selected vertical profile displayed in (b). Dashed line displays linear trend for all samples, grey box highlights samples used for Figures (c) and (d). **(b)** Age-elevation plot for samples FD020 to FD024 (southern Vosges Mountains) with error bars. Blue rhombi show AFT mean ages from Timar-Geng et al. (2006). Envelopes are based on minimum / maximum values for all grains (light grey) and for accepted grains (dark grey). Black outline defines vertical profile used for thermal modeling (see Fig. 7), uppermost samples have been excluded from thermal modeling due to a distinct increase in cooling ages between samples FD020 and FD021. **(c)** Weighted-mean age ($\bar{x}_w$) – distance plot for samples with a maximum elevation of 750 m. Distance is calculated against the WMBF and EMBF for the Vosges Mountains and Black Forest, respectively. **(d)** Weighted standard deviation (SD_w) – distance plot for samples with a maximum elevation of 750 m. Distance is calculated against the WMBF and EMBF for the Vosges Mountains and Black Forest, respectively. Dashed grey line represents a smoothed trend using a locally estimated scatterplot smoothing (LOESS) algorithm.

bustness. A subset of well-fitting models, which provide a more reliable representation of the thermal history, is shown in Figure 6.

Thermal models were calculated for individual samples and for one selected vertical profile (Figs. 6 and 7). All models start at initial temperatures of approximately 800 °C and show decreasing temperatures to near-surface values by the Triassic (225 ± 25 Ma, 10 ± 10 °C). During the Jurassic, model results indicate reheating of all samples into the apatite partial retention zone (PRZ), with temperatures between 60 and 90 °C (Fig. 6; Supplement S7). Modeled Cretaceous temperature paths display a wide range of maximum temperatures and uncertainties, ranging from ~70 °C (e.g., FD027) to ~135 °C (e.g., FD020).

During the Cretaceous, several samples record cooling at around 90 Ma. These samples are located at the highest elevations along the rift shoulders of the southern Black Forest (FD005), northern Black Forest (FD057), and the southern Vosges Mountains (FD020) (Fig. 6). Cooling rates derived from the thermal models range from relatively fast cooling of 6–10 °C Ma^{-1} over ~10 Ma (FD005, FD020) in the southern Black Forest and Vosges Mountains to slow and gradual cooling of ~0.7 °C Ma^{-1} from the Cretaceous to the present (FD057) in the northern parts of the mountain ranges. At the end of the Cretaceous (~70 Ma), a second cooling phase is recorded by four samples (FD026, FD033, FD038, FD054), showing temperature decreases of up to ~100 °C. Associated cooling rates range between ~5 and 7 °C Ma^{-1} for samples from the Vosges Mountains and the northern Black Forest.

During the Eocene, rapid cooling exceeding ~10 °C Ma^{-1} is observed in samples from the southern Black Forest (FD003), southern Vosges Mountains (FD030, FD032), northern Vosges Mountains (FD049, FD050), and northern Black Forest (FD062, FD064). These samples are mainly located near the highest elevations in the north-

ern Vosges Mountains and southern Black Forest. The remaining samples are characterized by high model uncertainty from the Cretaceous to the Miocene. Their thermal paths diverge later into slow Eocene cooling at rates of ~2 °C Ma^{-1} (FD014, FD055), rapid Eo-Oligocene cooling (~10 °C Ma^{-1}; FD037), or fast Miocene cooling reaching up to ~20 °C Ma^{-1} (FD013, FD015, FD027, FD064). A Cenozoic reheating phase is recorded in samples FD005 (Miocene) and FD064 (Late Eocene to Miocene), showing temperature increases of approximately 30 °C, followed by renewed cooling to surface temperatures during the Miocene to Quaternary.

The thermal history of the vertical profile at the Grand Ballon (Fig. 7) follows a similar time-temperature path to the individual samples. Even though model uncertainty increases during the Cretaceous, the modeled expected path reveals two distinct episodes of fast reheating followed by subsequent fast cooling during the Eocene. A temperature maximum of ~100 °C is reached during the Early Eocene (~55 Ma), followed by rapid cooling until ~50 Ma. A second, less pronounced reheating phase around 45 Ma raises temperatures to 60–90 °C, before rapid cooling resumes until ~40 Ma. Subsequent gradual cooling continues throughout the remaining Cenozoic to present-day surface temperatures.

5. Discussion

5.1. Regional age distribution

The newly acquired apatite (U-Th)/He data show a consistent spatial pattern of younger ages in immediate proximity to the Upper Rhine Graben. Cooling ages increase with increasing distance from the rift (Figs. 2, 4c, 4d, 5) as well as with increasing elevation (Figs. 3, 4a, 4b). This first-order pattern is especially evident in the southern Vosges Mountains and Black Forest and in previously published AFT and AHe data from this region (Fig. 5) (Link, 2009; Timar-Geng et al., 2006; Dresmann, 2009) and from other rift systems and passive continental margins (Wildman et al., 2019; Turab et al., 2023; Mansour et al., 2025; Boone et al., 2021; Su et al., 2021; Olivetti et al., 2020). In contrast, intra-sample age variability reaches a maximum at the rift flank and decreases again with increasing distance from the highest points (Fig. 4d). While calculated Eocene weighted-mean AHe ages are concentrated near the graben, samples from more distant locations yield weighted-mean cooling ages ranging from the Late Cretaceous to the Paleocene.

Two scenarios can explain these older weighted-mean cooling ages: either these samples experienced earlier cooling and were exhumed to temperatures below the partial retention zone already around ~65 Ma, or they never experienced sufficient temperature to fully reset their accumulated radiation damage and inherited helium. The latter scenario would result in partially reset ages from an even older phase.

The high single-grain age dispersion we observe in many samples supports the incomplete resetting hypothesis (Fig. 4d). This variability is a consequence of several factors, including radiation damage from the decay of U and Th, as well as inherited helium, inclusions, and U/Th zonation (Flowers et al., 2022a; Green and Duddy, 2018). Whereas the effect of low eU concentrations on radiation damage can be neglected, the effect of radiation damage on AHe ages with high eU concentrations has been shown to be significant, especially for slowly-cooled or reheated basement rocks and if there is no clear relationship between crystal ages and size (Gautheron et al., 2009). Both considerations are relevant to the samples analyzed in our thermal modeling.

High dispersion in AHe single-grain ages has been reported in various studies, including studies from Variscan massifs in Central Europe (Black Forest & Vosges Mountains: Link, 2009; Bohemian Massif: Hejl et al., 2023; Wolff et al., 2015; Massif Central: Gautheron et al., 2009; Olivetti et al., 2020). Even though these regions are separated by several hundreds of kilometers, these mountain ranges share a common Paleozoic crystallization and Mesozoic depositional history and have been uplifted again during the Cenozoic (e.g., Dremel et al., 2025). Interestingly, not all samples from these studies, including samples of this study, show a clear age – eU correlation, which would typically be expected if radiation damage had a systematic effect on closure temperatures (e.g., Flowers et al., 2022a, 2022b, 2009; Gautheron et al., 2009). This suggests either heterogeneous annealing histories, non-linear relationships between radiation damage and diffusion, or other internal factors (Beucher et al., 2013; Brown et al., 2013). These complexities are illustrated by the discrepancy between samples FD034 (Oligocene – Eocene) and FD038 (Paleocene – Cretaceous), which, despite being located at similar elevations and in close spatial proximity, yield different AHe ages (Figs. 1, 2, 4). FD034 is significantly younger than FD038, and within uncertainty has a comparable cooling age as FD064, located at the far northeastern margin of the Black Forest. This potentially indicates localized influences such as hydrothermal activity (Link, 2009; Dresmann, 2009). Within the Black Forest and further to the southeast, it has been shown that AHe data are influenced by hydrothermal activity, explaining some of the observed single-grain age dispersion (Link, 2009; Frings et al., 2025). In contrast, sample FD064 displays the youngest age (Miocene) in the dataset with notably low dispersion, despite being derived from Triassic sandstone and no immediate proximity to faults. Due to decreasing flexural strain with increasing distance from the graben, the density of rift-related normal faults progressively decreases (e.g., Dremel et al., 2025; Bott, 1992; Knott et al., 1996; Weissel and Karner, 1989). Since the effect of hydrothermal fluids on low-temperature thermochronology is predominantly focused along fault zones (Lupi et al., 2010; Dresmann et al., 2010), their decreasing abundance away from the rift implies a reduction in hydrothermal activity and associated thermal overprint. This spatial trend likely contributes to the observed cooling age distribution, with stronger hydrothermal influence in the

immediate vicinity of the graben that decreases with increasing distance (Fig. 4c). As a result, the expected decrease in hydrothermal activity with distance from the URG likely leads to a reduced spread in cooling ages in areas farther from the rift flank (Fig. 4d).

Samples FD003, FD005, FD013, FD015, FD026, and FD030 were collected from outcrops that have previously been dated using AFT thermochronology (Fig. 1) (Timar-Geng et al., 2006). When directly comparing AFT and AHe ages, the AHe ages range from being 36 % younger up to 282 % older, i.e., nearly threefold the age of AFT data. Thermal history models derived from the AFT data (Timar-Geng et al., 2006) and the AHe data from this study indicate broadly similar cooling trends during the Cretaceous. In contrast, the Paleogene thermal evolution differs markedly: AHe models mainly remain below ~40 °C (except FD005 and FD015), whereas AFT models suggest coherent Oligocene reheating to temperatures of up to ~100 °C, followed by rapid Miocene cooling to near-surface conditions. During the Miocene, AFT models consistently record rapid cooling, whereas several AHe models indicate limited or no additional cooling after remaining at low temperatures. Notably, this Paleogene reheating was already discussed by Timar-Geng et al. (2006) as potentially reflecting modeling artefacts related to the need to reproduce shortened fission-track lengths.

Especially samples FD015 and FD026 yielded consistently younger ages than their corresponding AFT counterparts, suggesting a Miocene and Paleocene thermal overprint, respectively. An inverted age distribution is most pronounced in the Black Forest and diminishes progressively towards the graben. A similar pattern, where AHe ages exceed AFT ages, has been reported previously in this region (Link, 2009), other Variscan massifs (Olivetti et al., 2020; Hejl et al., 2023), and other continental rift settings (e.g., Turab et al., 2023; Mansour et al., 2025; Su et al., 2021). Possible explanations for such inverted profiles are crystal-scale effects on the cooling ages (e.g., radiation damage, U-Th zonation or implantation, micro-inclusions, radiation-enhanced annealing) or long residence times within the PRZ.

In summary, the spatial and intra-sample variability of AHe ages in the Black Forest & Vosges Mountains reflects a complex interplay between exhumation timing, variable thermal overprinting, and crystal-scale controls on helium diffusion. By combining new AHe measurements with published AFT data, we obtained a more robust reconstruction of the thermal history, especially for the younger Cenozoic. Targeted sampling along several profiles perpendicular to the rift axis further allowed us to distinguish multiple cooling phases, which can be directly linked to episodes of uplift and exhumation that affected the region. Additionally, the high spatial resolution of these profiles offers new insights into localized processes, such as hydrothermal fluid flow in the vicinity of normal faults.

5.2. Mesozoic and Cenozoic thermal history

Burial-related heating affected the crust during the Triassic and Jurassic, as approximately 1000–1500 m of sediments were deposited (~450–650 m during the Triassic and ~700 m during the Jurassic) (Figs. 6 and 7, Supplement S7) (e.g., Häring, 2002; Wetzel et al., 2003; Geyer and Gwinner, 1991). In contrast, the absence of preserved Cretaceous sediments leaves their existence debated, either reflecting a phase of non-deposition and erosion of Jurassic and Triassic sediments or an unconstrained amount of deposition followed by subsequent erosion (e.g., Dresmann, 2009; Ziegler and Dèzes, 2007; Geyer and Gwinner, 1991).

The widespread preservation of these Triassic and Jurassic units, both in elevated structural positions and along the margins of the Vosges Mountains and Black Forest, along with their presence in the graben itself, implies regionally extensive sediment accumulation (Häring, 2002; Hinsken et al., 2007; Ziegler and Dèzes, 2007). However, hydrothermal activity and heat anomalies also affected the region during this phase, as reported by vein mineralizations, ZFT and AHe data (Wetzel et al., 2003; Link, 2009; Timar-Geng et al., 2006; Frings et al., 2025).

During the Cretaceous, the temperature uncertainty increases for most samples except FD027. Several thermal models show an expected thermal stability during this period (Figs. 6 and 7). This is in line with ongoing hydrothermal activity (Wetzel et al., 2003), measured cooling ages from this study (e.g., FD005, FD020, FD054, and FD057), and data from literature (Timar-Geng et al., 2006; Link, 2009; Frings et al., 2025).

Early Cretaceous cooling events (~130 Ma), previously identified in published apatite fission-track datasets from adjacent regions and interpreted as large-scale domal uplift (Olivetti et al., 2020; Barbarand et al., 2018; Link, 2009; Ziegler and Dèzes, 2007), are not recorded in this dataset. This absence may indicate that any cooling in the study area was too minor to be resolved by the current thermochronological dataset, potentially falling below the sensitivity limits of apatite (U-Th)/He. Alternatively, it is possible that significant local cooling simply did not occur, highlighting the potential for spatial heterogeneity in Early Cretaceous thermal histories across the rift flanks. However, a second Cretaceous cooling phase (~90–70 Ma), linked to intraplate compression, basin inversion, and basement thrusting associated with the convergence of Africa, Iberia, and Europe (Kley and Voigt, 2008), is evident in several thermal histories from both the Black Forest and Vosges Mountains, particularly in samples from high elevations along the southern and northern transects (Figs. 6 and 7). Subsequent thermal relaxation of the isotherms resulted in a renewed cooling phase, which occurred over a million-year time scale, as evidenced by hydrothermal vein mineralization and thermal models (Wetzel et al., 2003; Timar-Geng et al., 2006; Link, 2009) and has been correlated with marine sedimentation during the Cenomanian transgression (Briais

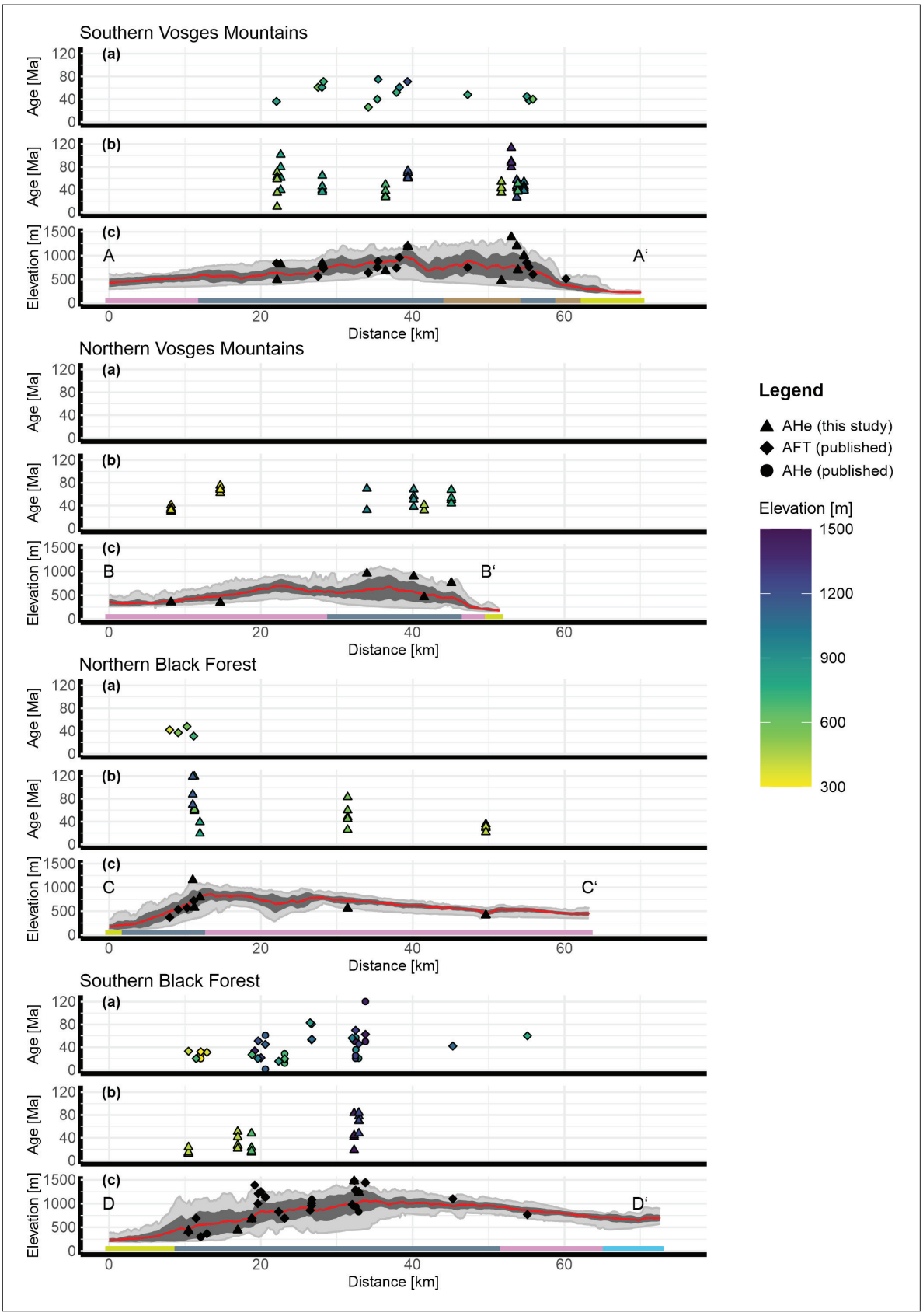

Figure 5: (a) Published AFT ages (rhombi) and AHe single-grain ages (circles) plotted against distance along profiles and color-coded according to sample elevation. **(b)** AHe single-grain ages (triangles) from this study plotted against distance along profiles and color-coded according to sample elevation. **(c)** Swath profiles with a swath width of 10 km. AFT and AHe samples are plotted at their respective elevation. Locations of swath profiles are marked as dashed lines in Figure 1b. Profiles are shown as mean (red line), 1σ (dark grey), and minimum/maximum (light grey). Colored bar at the bottom depicts chronostratigraphic age from Asch (2003, IGME 5000, BGR) (Fig. 1c).

et al., 2025). However, because most samples remained below the PRZ temperature range for extended periods, Cenozoic exhumation must have been limited, whereas elevated temperature gradients associated with hydrothermal fluid flow near fault zones led to largely localized thermal overprinting (Dresmann, 2009; Link, 2009).

Reheating at the Cretaceous-Paleocene transition (~65 Ma) coincides with a phase of widespread intraplate compression, uplift, and basin inversion in the Alpine and Pyrenean forelands, including the future Upper Rhine Graben region (Dèzes et al., 2004; Ziegler, 1990; Ziegler and Dèzes, 2007). These processes are attributed to far-field stress transmission related to ongoing Alpine convergence and were accompanied by mantle-derived magmatism and lithospheric thermal weakening (Wilson et al., 1995; Ziegler et al., 1995; Merle, 2011; Granet et al., 1995). Rather than marking the onset of rifting, this phase likely represents a pre-rift thermal and mechanical conditioning of the lithosphere that facilitated later Eocene – Oligocene extension in the Upper Rhine Graben (Sengör, 1976; Schumacher, 2002; Brune et al., 2023).

Following a Paleocene-Eocene thermal peak, a phase of rapid cooling (~65 °C within ~2 Ma) coincided with flexural uplift of the rift flanks (Ziegler and Dèzes, 2007; Grimmer et al., 2017; Berger et al., 2005). The vertical profile spans more than 700 m in elevation (Fig. 4), and the presence of Eocene AFT and AHe ages throughout the profile indicates that rock uplift during this rifting phase must have exceeded this amount. Although this cooling signal is broadly consistent across the profile, closer inspection of the age-elevation relationship reveals a significant deviation from a simple monotonic trend. A pronounced step in both elevation and cooling age between samples FD021 and FD020 is interpreted as a preserved fossil apatite partial retention zone (PRZ). Rather than reflecting syn-rift thermal resetting, this feature is interpreted to represent a pre-rift thermal structure that was subsequently exhumed during Eocene rift flank uplift. This implies that not all samples within the vertical profile shared a common pre-exhumation thermal history. Consequently, sample FD020, likely residing above the pre-rift PRZ prior to rifting, was excluded from the vertical profile used for inverse thermal modeling.

This phase of rapid cooling and uplift during the Eocene is associated with increased erosion and exhumation of the Variscan basement, driven by the removal of overlying, easily erodible Mesozoic sedimentary cover (Timar-Geng et al., 2006; Ziegler and Dèzes, 2007). Based on combined AFT and AHe thermal modeling (Fig. 7), exhumation of approximately 1500 m over ~5 Ma is inferred for this period, assuming a constant paleo-geothermal gradient of 45 °C km^{-1}. This estimate is consistent with independent constraints on sediment thickness and erosion derived from regional stratigraphic and structural studies (Geyer and Gwinner, 1991; Dresmann et al., 2010; Timar-Geng et al., 2006; Häring, 2002; Lutz and Cleintuar, 1999). However, these calculations are only valid under the assumption of stable geothermal gradients, an assumption that has to be questioned due to variable local (20–100 °C km^{-1}) and paleo-geothermal gradients (Schellschmidt and Clauser, 1996; Häring, 2002; Timar-Geng et al., 2006; Dresmann, 2009; Link, 2009).

After the initial rifting of the URG during the Eocene and Oligocene, the region was affected by large-scale crustal deformation, with continued activity along rift-related faults. During the Miocene, differential vertical motion between the graben and its shoulders led to rift-flank uplift in the southern URG that outpaced extensional subsidence, resulting in relative exhumation of the Variscan basement along the graben shoulders. This uplift appears to be more pronounced in the southern URG, where lithospheric folding has been proposed to have contributed to enhanced vertical motions. In contrast, the northern URG continued to subside along active fault systems, highlighting the spatial variability of vertical motions within the rift (Ziegler and Dèzes, 2007). In total, rift-flank uplift over the last 25 Ma is estimated to be on the order of ~1 km, although this value remains poorly constrained (Grimmer et al., 2017; Link, 2009). Previous studies based on AFT and AHe data observed several low magnitude phases of heating and subsequent cooling since the Oligo-Miocene (Link, 2009; Timar-Geng et al., 2006). To account for shortened apatite fission-tracks, previous thermal models invoked a Miocene reheating event in most samples from the URG and adjacent mountain ranges, with temperature increases of 20–40 °C to maximum values of 60–90 °C (Timar-Geng et al., 2006; Dresmann, 2009; Link, 2009). Following this reheating, temperatures progressively cooled to near-surface conditions from the Miocene to the present. However, this Miocene event was interpreted either as regional-scale surface uplift accompanied by erosion, or as modeling artifacts (Link, 2009; Timar-Geng et al., 2006). In contrast, AHe data from this study do not support regionally extensive Miocene reheating, as such a signal is only recorded in samples located in the immediate vicinity of normal faults, whereas shortened AFT tracks are reported from samples across both rift flanks, well beyond the vicinity of active fault zones. Therefore, we interpret these as fossil tracks that were partially annealed during reheating associated with the Late Cretaceous – Paleocene thermal maximum, without exceeding the upper PAZ limit of ~120 °C (e.g., Green et al., 1986; Ketcham, 2019). Consistent with this interpretation, temperatures around 65 Ma likely approached ~120 °C – barely sufficient to fully anneal pre-existing radiation damage in apatite – and may thus account for the pronounced dispersion of many AHe ages, particularly in samples beyond the immediate rift shoulders where annealing remained incomplete (e.g., Gautheron et al., 2009).

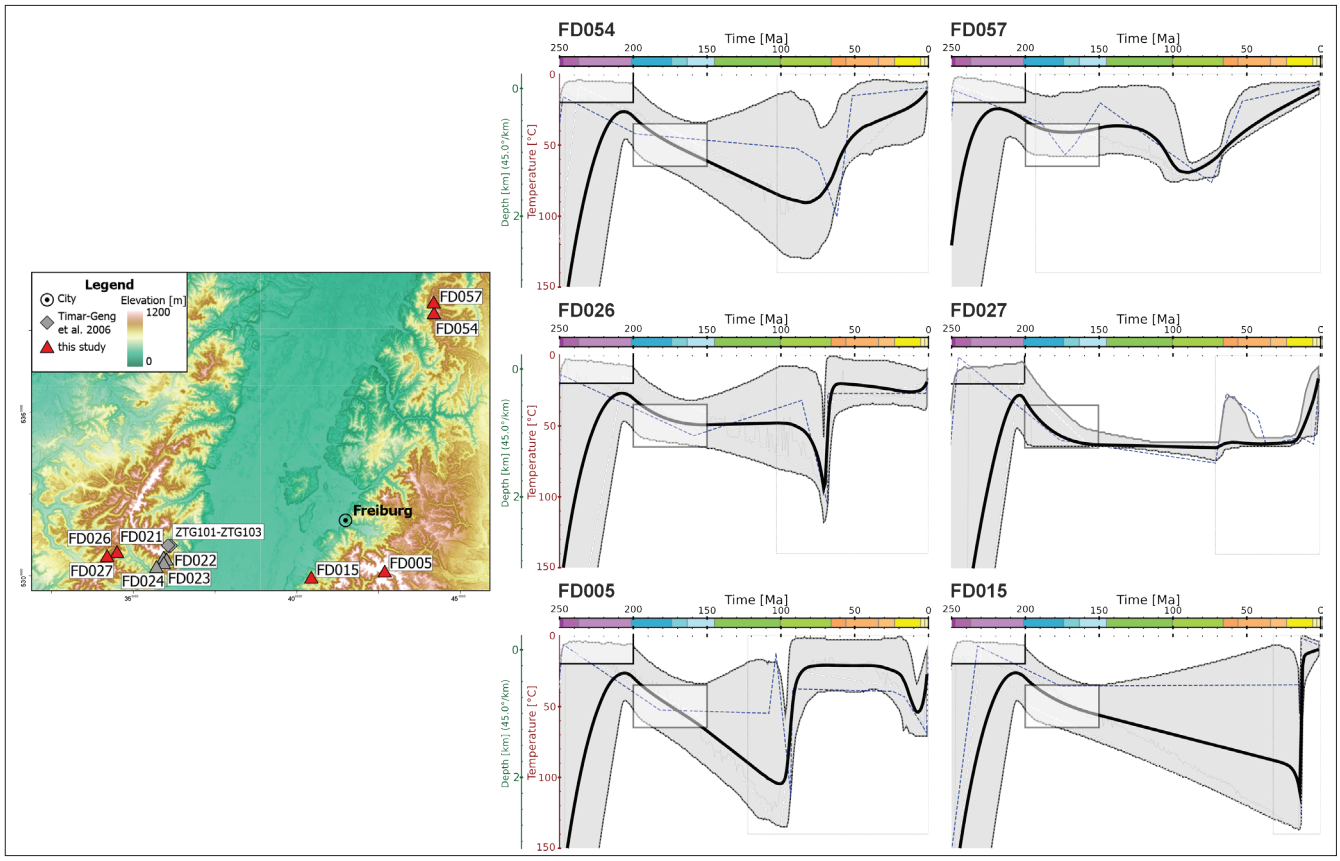

Figure 6: Thermal models for selected samples. Locations are annotated according to sample number. Thermal histories have been restricted to a maximum age of 250 Ma and 150 °C. Paths are shown as 96 % envelop for all paths (grey), expected path (black), and max likelihood (dashed blue).

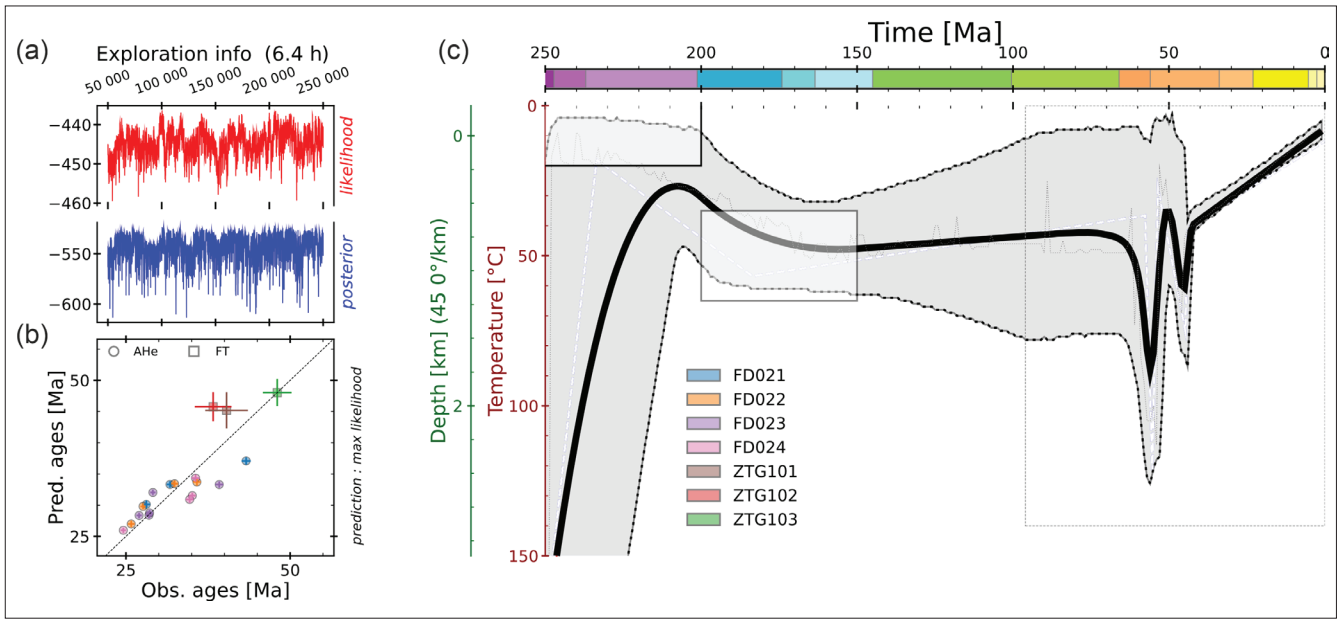

Figure 7: Thermal model for vertical profile including AHe samples FD021 – FD024 and AFT data ZTG101 – ZTG103 (Timar-Geng et al., 2006). Sample locations are shown in Fig. 6. (a) plot depicts likelihood (red) and posterior (blue), (b) plot shows observed ages vs predicted ages, with samples color-coded according to the legend displayed within the thermal history model (c) thermal history is restricted to a maximum age of 250 Ma and a maximum temperature of 150 °C. Thermal constraints are shown as black boxes, grey area displays 96 % envelop for all paths, including the expected path in black. Thermal history reveals an increasing uncertainty towards the Late Cretaceous, with a distinct heating pulse during the Paleocene (~60 Ma) and a second pulse during the Eocene (50 – 45 Ma), followed by slow and gradual cooling.

6. Conclusion

This study adds 113 new single-grain apatite (U-Th)/He ages from 26 samples to the thermochronological record of the Black Forest and Vosges Mountains, covering a range of 10.3 ± 0.6 to 179.5 ± 11.7 Ma, and enabling a refined reconstruction of their post-Jurassic thermal history. The dataset confirms a first-order spatial pattern of young, consistent ages near the Upper Rhine Graben and older, more dispersed ages with increasing distance and elevation.

High intra-sample age dispersion, observed across much of the dataset, reflects incomplete resetting of helium due to insufficient annealing of radiation damage, inherited helium, and crystal-scale heterogeneities. Localized hydrothermal overprint near active faults further contributes to variability, emphasizing the importance of spatially resolved sampling.

Thermal models and age patterns corroborate multiple cooling and heating phases: (i) a Late Cretaceous cooling linked to intraplate compression and basin inversion; (ii) renewed reheating around the Cretaceous – Paleocene transition, associated with the onset of rifting and Alpine coupling, likely raising temperatures close to the upper PAZ limit (~120 °C) without full resetting; and (iii) rapid Eocene cooling connected to flexural uplift and significant basement exhumation. In contrast, widespread Miocene reheating to temperatures > 60 °C is not supported by our data and is better explained by earlier partial annealing during the Late Cretaceous – Paleocene maximum temperatures predicted by the thermal models (~100–150 °C) and localized hydrothermal overprinting.

Overall, the Black Forest – Vosges Mountains record illustrates how regional tectonic phases, transient thermal overprints, and crystal-scale processes combine to produce heterogeneous thermochronological signatures. By integrating AHe with AFT data along spatially resolved transects, this study demonstrates their potential to unravel complex thermal histories in slowly exhuming intraplate settings.

Supplementary data

Supplementary material (S1–S7) associated with this article are online available on Zenodo: https://doi.org/10.5281/zenodo.18661110.

Acknowledgements

We thank Kurt Stüwe for editorial handling and Anke Friedrich and Christoph Glotzbach for their constructive and insightful reviews, which helped to improve the clarity and quality of this manuscript. This study was supported by the University of Salzburg and is associated with the research project ThinkALPS (HA7660/6-1) within the DFG priority program "Mountain Building in 4-D".

References

Abbey A.L., Wildman M., Stevens Goddard A.L., Murray K.E., 2023. Thermal history modeling techniques and interpretation strategies: Applications using QTQt. Geosphere 19, 493–530. https://doi.org/10.1130/GES02528.1

Asch K., 2003. The 1:5 Million International Geological Map of Europe and Adjacent Areas: Development and Implementation of a GIS-enabled Concept, 1. Edition. ed, Geologisches Jahrbuch. E. Schweizerbart'sche Verlagsbuchhandlung, Stuttgart.

Barbarand J., Bour I., Pagel M., Quesnel F., Delcambre B., Dupuis C., Yans J., 2018. Post-Paleozoic evolution of the northern Ardenne Massif constrained by apatite fission-track thermochronology and geological data. BSGF – Earth Sciences Bulletin 189, 16. https://doi.org/10.1051/bsgf/2018015

Beucher R., Brown R.W., Roper S., Stuart F., Persano C., 2013. Natural age dispersion arising from the analysis of broken crystals: Part II. Practical application to apatite (U-Th)/He thermochronometry. Geochimica et Cosmochimica Acta 120, 395–416. https://doi.org/10.1016/j.gca.2013.05.042

Bishop P., 2007. Long-term landscape evolution: linking tectonics and surface processes. Earth Surface Processes and Landforms 32, 329–365. https://doi.org/10.1002/esp.1493

Boone S.C., Balestrieri M.-L., Kohn B., 2021. Tectono-Thermal Evolution of the Red Sea Rift. Frontiers in Earth Science 9. https://doi.org/10.3389/feart.2021.713448

Bosworth W., 1985. Geometry of propagating continental rifts. Nature 316, 625–627. https://doi.org/10.1038/316625a0

Bott M.H.P., 1992. Modelling the loading stresses associated with active continental rift systems. Tectonophysics 215, 99–115. https://doi.org/10.1016/0040-1951(92)90076-I

BRGM, 2025. Geoservices BRGM: WMS-C Services.

Briais J., Barbarand J., Lasseur E., Homberg C., Allanic C., Bellahsen N., Carter A., Chateauneuf J.-J., Beccaletto L., Jolivet L., Ourliac C., 2025. Thermal and Tectono-Sedimentary Record of the Upper Rhine Graben (Cretaceous to Oligocene): Oblique Rifting Development Influenced by Pre-Rift Thermicity and Far Field Stress. https://doi.org/10.2139/ssrn.5351701

Brown R.W., Beucher R., Roper S., Persano C., Stuart F., Fitzgerald P., 2013. Natural age dispersion arising from the analysis of broken crystals. Part I: Theoretical basis and implications for the apatite (U-Th)/He thermochronometer. Geochimica et Cosmochimica Acta 122, 478–497. https://doi.org/10.1016/j.gca.2013.05.041

Brune S., Kolawole F., Olive J.-A., Stamps D.S., Buck W.R., Buiter S.J.H., Furman T., Shillington D.J., 2023. Geodynamics of continental rift initiation and evolution. Nature Reviews Earth & Environment 4, 235–253. https://doi.org/10.1038/s43017-023-00391-3

Cooperdock E.H.G., Ketcham R.A., Stockli, D.F., 2019. Resolving the effects of 2-D versus 3-D grain measurements on apatite (U-Th) / He age data and reproducibility. Geochronology 1, 17–41. https://doi.org/10.5194/gchron-1-17-2019

Dèzes P., Schmid S.M., Ziegler P.A., 2004. Evolution of the European Cenozoic Rift System: interaction of the Alpine and Pyrenean orogens with their foreland lithosphere. Tectonophysics 389, 1–33. https://doi.org/10.1016/j.tecto.2004.06.011

Dremel F., Robl J., Hergarten S., Villamizar-Escalante N., Friedrichs B., von Hagke C., 2025. Old orogens – young topography: Characterizing styles of late Cenozoic uplift and exhumation in the European Variscan belt. Geomorphology. https://doi.org/10.1016/j.geomorph.2025.110001

Dresmann H., 2009. Fission-Track analyses in the area of the southern Upper Rhine Graben (Dissertation). Universität Basel, Basel.

Dresmann H., Keulen N., Timar-Geng Z., Fügenschuh B., Wetzel A., Stünitz H., 2010. The south-western Black Forest and the Upper Rhine Graben Main Border Fault: thermal history and hydrothermal fluid flow. International Journal of Earth Sciences 99, 285–297. https://doi.org/10.1007/s00531-008-0391-3

Ehlers T.A., Farley K.A., 2003. Apatite (U-Th)/He thermochronometry: methods and applications to problems in tectonic and surface processes. Earth and Planetary Science Letters 1–14.

Farley K.A., 2002. (U-Th)/He Dating: Techniques, Calibrations, and Applications. Reviews in Mineralogy and Geochemistry 47, 819–844. https://doi.org/10.2138/rmg.2002.47.18

Flowers R.M., Ketcham R.A., Enkelmann E., Gautheron C., Reiners P.W., Metcalf J.R., Danišík M., Stockli D.F., Brown R.W., 2022a. (U-Th)/He chronology: Part 2. Considerations for evaluating, integrating, and interpreting conventional individual aliquot data. GSA Bulletin. https://doi.org/10.1130/B36268.1

Flowers R.M., Ketcham R.A., Shuster D.L., Farley K.A., 2009. Apatite (U-Th)/He thermochronometry using a radiation damage accumulation and annealing model. Geochimica et Cosmochimica Acta 73, 2347–2365. https://doi.org/10.1016/j.gca.2009.01.015

Flowers R.M., Zeitler P.K., Danišík M., Reiners P.W., Gautheron C., Ketcham R.A., Metcalf J.R., Stockli D.F., Enkelmann E., Brown R.W., 2022b. (U-Th)/He chronology: Part 1. Data, uncertainty, and reporting. GSA Bulletin. https://doi.org/10.1130/B36266.1

Frings K.A., Madritsch H., Villamizar-Escalante N., Kukla P.A., von Hagke, C., 2025. Using the Dispersion of Apatite (U-Th-Sm)/He Single Grain Ages to Unravel the Burial and Exhumation History of the Foreland Basin of the Central Alps. Basin Research 37. https://doi.org/10.1111/bre.70056

Fuhrmann T., Heck B., Knöpfler A., Masson F., Mayer M., Ulrich P., Westerhaus M., Zippelt K., 2013. Recent surface displacements in the Upper Rhine Graben – Preliminary results from geodetic networks. Tectonophysics 602, 300–315. https://doi.org/10.1016/j.tecto.2012.10.012

Gallagher K., 2012. Transdimensional inverse thermal history modeling for quantitative thermochronology. Journal of Geophysical Research 117. https://doi.org/10.1029/2011JB008825

Gautheron C., Tassan-Got L., Barbarand J., Pagel M., 2009. Effect of alpha-damage annealing on apatite (U-Th)/He thermochronology. Chemical Geology 266, 157–170. https://doi.org/10.1016/j.chemgeo.2009.06.001

Geyer O.F., Gwinner M.P., 1991. Geologie von Baden-Württemberg, 4th ed. ed. Schweizerbart, Stuttgart.

Giamboni M., Ustaszewski K., Schmid S.M., Schumacher M.E., Wetzel A., 2004a. Plio-Pleistocene transpressional reactivation of Paleozoic and Paleogene structures in the Rhine-Bresse transform zone (northern Switzerland and eastern France). International Journal of Earth Sciences 93, 207–223. https://doi.org/10.1007/s00531-003-0375-2

Giamboni M., Wetzel A., Nivière B., Schumacher M., 2004b. Plio-Pleistocene folding in the southern Rhinegraben recorded by the evolution of the drainage network (Sundgau area; northwestern Switzerland and France). Eclogae Geologicae Helvetiae 97, 17–31. https://doi.org/10.1007/s00015-004-1112-4

Granet M., Wilson M., Achauer U., 1995. Imaging a mantle plume beneath the French Massif Central. Earth and Planetary Science Letters 281–296.

Green P., Duddy I., 2018. Apatite (U-Th-Sm)/He thermochronology on the wrong side of the tracks. Chemical Geology 488, 21–33. https://doi.org/10.1016/j.chemgeo.2018.04.028

Green P.F., Duddy I.R., Gleadow A.J.W., Tingate P.R., Laslett G.M., 1986. Thermal annealing of fission tracks in apatite. Chemical Geology: Isotope Geoscience section 59, 237–253. https://doi.org/10.1016/0168-9622(86)90074-6

Grimmer J.C., Ritter J.R.R., Eisbacher G.H., Fielitz W., 2017. The Late Variscan control on the location and asymmetry of the Upper Rhine Graben. International Journal of Earth Sciences 106, 827–853. https://doi.org/10.1007/s00531-016-1336-x

Häring M., 2002. Sondierbohrung Otterbach, Basel. Der erste Schritt zur Entwicklung eines geothermischen Heiz-Kraftwerks nach dem Hot-Dry-Rock Verfahren. Bulletin für Angewandte Geologie 19–30.

Hejl E., Heberer B., Salcher B., Sekyra G., Van den haute P., Leichmann J., 2023. Thermochronological constraints on the post-Variscan exhumation history of the southeastern Bohemian Massif (Waldviertel and Weinsberg Forest, Austria): palaeogeographic and geomorphologic implications. International Journal of Earth Sciences. https://doi.org/10.1007/s00531-023-02294-6

Hinsken S., Ustaszewski K., Wetzel A., 2007. Graben width controlling syn-rift sedimentation: the Palaeogene southern Upper Rhine Graben as an example. International Journal of Earth Sciences 96, 979–1002. https://doi.org/10.1007/s00531-006-0162-y

Illies J.H., 1972. The Rhine graben rift system-plate tectonics and transform faulting. Geophysical Surveys 1, 27–60. https://doi.org/10.1007/BF01449550

Ketcham R.A., 2019. Fission-Track Annealing: From Geologic Observations to Thermal History Modeling, in: Malusà, M.G., Fitzgerald, P.G. (Eds.), Fission-Track Thermochronology and Its Application to Geology, Springer Textbooks in Earth Sciences, Geography and Environment. Springer International Publishing, Cham, 49–75. https://doi.org/10.1007/978-3-319-89421-8_%25203

Ketcham R.A., 2005. Forward and Inverse Modeling of Low-Temperature Thermochronometry Data. Reviews in Mineralogy and Geochemistry 58, 275–314. https://doi.org/10.2138/rmg.2005.58.11

Ketcham R.A., Gautheron, C., Tassan-Got, L., 2011. Accounting for long alpha-particle stopping distances in (U-Th-Sm)/He geochronology: Refinement of the baseline case. Geochimica et Cosmochimica Acta 75, 7779–7791. https://doi.org/10.1016/j.gca.2011.10.011

Kettermann M., Weismüller C., von Hagke C., Reicherter K., Urai J.L., 2019. Large near-surface block rotations at normal faults of the Iceland rift: Evolution of tectonic caves and dilatancy. Geology 47, 781–785. https://doi.org/10.1130/G46158.1

Kley J., Voigt T., 2008. Late Cretaceous intraplate thrusting in central Europe: Effect of Africa-Iberia-Europe convergence, not Alpine collision. Geology 36, 839. https://doi.org/10.1130/G24930A.1

Knott S.D., Beach A., Brockbank P.J., Lawson Brown J., McCallum J.E., Welbon A.I., 1996. Spatial and mechanical controls on normal fault populations. Journal of Structural Geology 18, 359–372. https://doi.org/10.1016/S0191-8141(96)80056-3

Kroner U., Romer R.L., 2013. Two plates – Many subduction zones: The Variscan orogeny reconsidered. Gondwana Research 24, 298–329. https://doi.org/10.1016/j.gr.2013.03.001

Link K., 2009. Die thermo-tektonische Entwicklung des Oberrheingraben-Gebietes seit der Kreide (Dissertation). Uni Freiburg, Freiburg i.Br.

Lupi M., Geiger S., Graham C.M., 2010. Hydrothermal fluid flow within a tectonically active rift-ridge transform junction: Tjörnes Fracture Zone, Iceland. Journal of Geophysical Research 115. https://doi.org/10.1029/2009JB006640

Lutz M., Cleintuar M., 1999. Geological results of a hydrocarbon exploration campaign in the southern Upper Rhine Graben. Bulletin für Angewandte Geologie, 3–80.

Lysak S.V., 1992. Heat flow variations in continental rifts. Tectonophysics 208, 309–323. https://doi.org/10.1016/0040-1951(92)90352-7

Mancktelow N.S., Grasemann B., 1997. Time-dependent effects of heat advection and topography on cooling histories during erosion. Tectonophysics 270, 167–195. https://doi.org/10.1016/S0040-1951(96)00279-X

Mansour S., Hasebe N., Abdelrahman K., Fnais M.S., Tamura A., 2025. The Gulf of Suez rifting: implications from low-temperature thermochronology. International Geology Review 67, 694–710. https://doi.org/10.1080/00206814.2024.2400695

Matte P., 2001. The Variscan collage and orogeny (480–290 Ma) and the tectonic definition of the Armorica microplate: a review. Terra Nova 122–128.

Matte P., 1986. Tectonics and plate tectonics model for the Variscan belt of Europe. Tectonophysics 126, 329–374. https://doi.org/10.1016/0040-1951(86)90237-4

McDowell F.W., McIntosh W.C., Farley K.A., 2005. A precise 40Ar-39Ar reference age for the Durango apatite (U-Th)/He and fission-track dating standard. Chemical Geology 214, 249–263. https://doi.org/10.1016/j.chemgeo.2004.10.002

Merle O., 2011. A simple continental rift classification. Tectonophysics 513, 88–95. https://doi.org/10.1016/j.tecto.2011.10.004

Miller C.S., Baranyi V., 2021. Triassic Climates, in: Encyclopedia of Geology. Elsevier, 514–524. https://doi.org/10.1016/B978-0-12-409548-9.12070-6

Neuharth D., Brune S., Wrona T., Glerum A., Braun J., Yuan X., 2022. Evolution of Rift Systems and Their Fault Networks in Response to Surface Processes. Tectonics 41. https://doi.org/10.1029/2021TC007166

Olivetti V., Balestrieri M.L., Godard V., Bellier O., Gautheron C., Valla P.G., Zattin M., Faccenna, C., Pinna-Jamme R., Manchuel K., 2020. Cretaceous and late Cenozoic uplift of a Variscan Massif: The case of the French Massif Central studied through low-temperature thermochronometry. Lithosphere 12, 133–149. https://doi.org/10.1130/L1142.1

Piña-Valdés J., Socquet A., Beauval C., Doin M., D'Agostino N., Shen Z., 2022. 3D GNSS Velocity Field Sheds Light on the Deformation Mechanisms in Europe: Effects of the Vertical Crustal Motion on the Distribution of Seismicity. Journal of Geophysical Research: Solid Earth 127. https://doi.org/10.1029/2021JB023451

Regierungspräsidium Freiburg, 2021. LGRB-Kartenviewer.

Reiners P.W., 2005. Past, Present, and Future of Thermochronology. Reviews in Mineralogy and Geochemistry 58, 1–18. https://doi.org/10.2138/rmg.2005.58.1

Rohrman M., Van Der Beek P., Andriessen P., 1994. Syn-rift thermal structure and post-rift evolution of the Oslo Rift (southeast Norway): New constraints from fission track thermochronology. Earth and Planetary Science Letters 127, 39–54. https://doi.org/10.1016/0012-821X(94)90196-1

Rosendahl B.R., 1987. Architecture of Continental Rifts with Special Reference to East Africa. Annual Review of Earth and Planetary Sciences 15, 445–503. https://doi.org/10.1146/annurev.ea.15.050187.002305

Rotstein Y., Edel J.-B., Gabriel G., Boulanger D., Schaming M., Munschy M., 2006. Insight into the structure of the Upper Rhine Graben and its basement from a new compilation of Bouguer Gravity. Tectonophysics 425, 55–70. https://doi.org/10.1016/j.tecto.2006.07.002

Rotstein Y., Schaming M., 2008. Tectonic implications of faulting styles along a rift margin: The boundary between the Rhine Graben and the Vosges Mountains. Tectonics 27. https://doi.org/10.1029/2007TC002149

Saspiturry N., Lahfid A., Baudin T., Guillou-Frottier L., Razin P., Issautier B., Le Bayon B., Serrano, O., Lagabrielle Y., Corre B., 2020. Paleogeothermal Gradients Across an Inverted Hyperextended Rift System: Example of the Mauléon Fossil Rift (Western Pyrenees). Tectonics 39. https://doi.org/10.1029/2020TC006206

Schaltegger U., 2000. U-Pb geochronology of the Southern Black Forest Batholith (Central Variscan Belt): timing of exhumation and granite emplacement. International Journal of Earth Sciences 814–828. https://doi.org/10.1007/s005310050308

Schellschmidt R., Clauser C., 1996. The thermal regime of the Upper Rhine Graben and the Anomaly of Soultz. Zeitschrift für angewandte Geologie 40–44.

Schumacher M.E., 2002. Upper Rhine Graben: Role of preexisting structures during rift evolution. Tectonics 21, 6-1-6-17. https://doi.org/10.1029/2001TC900022

Sengör A.M.C., 1976. Collision of irregular continental margins: Implications for foreland deformation of Alpine-type orogens. Geol 4, 779.

Serpelloni E., Faccenna C., Spada G., Dong D., Williams S.D.P., 2013. Vertical GPS ground motion rates in the Euro-Mediterranean region: New evidence of velocity gradients at different spatial scales along the Nubia-Eurasia plate boundary. Journal of Geophysical Research: Solid Earth 118, 6003–6024. https://doi.org/10.1002/2013JB010102

Shuster D.L., Farley K.A., Sisterson J.M., Burnett D.S., 2004. Quantifying the diffusion kinetics and spatial distributions of radiogenic 4He in minerals containing proton-induced 3He. Earth and Planetary Science Letters 217, 19–32. https://doi.org/10.1016/S0012-821X(03)00594-6

Shuster D.L., Flowers R.M., Farley K.A., 2006. The influence of natural radiation damage on helium diffusion kinetics in apatite. Earth and Planetary Science Letters 249, 148–161. https://doi.org/10.1016/j.epsl.2006.07.028

Starostenko V.I., Danilenko V.A., Vengrovitch D.B., Kutas R.I., Stovba S.M., Stephenson R.A., Kharitonov O.M., 1999. A new geodynamical-thermal model of rift evolution, with application to the Dnieper-Donets Basin, Ukraine. Tectonophysics 313, 29–40. https://doi.org/10.1016/S0040-1951(99)00188-2

Sternai P., Sue C., Husson L., Serpelloni E., Becker T.W., Willett S.D., Faccenna C., Di Giulio A., Spada G., Jolivet L., Valla P., Petit C., Nocquet J.-M., Walpersdorf A., Castelltort S., 2019. Present-day uplift of the European Alps: Evaluating mechanisms and models of their relative contributions. Earth-Science Reviews 190, 589–604. https://doi.org/10.1016/j.earscirev.2019.01.005

Stüwe K., White L., Brown R., 1994. The influence of eroding topography on steady-state isotherms. Application to fission track analysis. Earth and Planetary Science Letters 124, 63–74. https://doi.org/10.1016/0012-821X(94)00068-9

Su P., He H., Tan X., Liu Y., Shi F., Kirby E., 2021. Initiation and Evolution of the Shanxi Rift System in North China: Evidence From Low-Temperature Thermochronology in a Plate Reconstruction Framework. Tectonics 40. https://doi.org/10.1029/2020TC006298

Timar-Geng Z., 2006. Post-Variscan thermal evolution of the flanks of the southern Upper Rhine Graben: fission-track analyses and thermal modelling (Dissertation). Universität Basel, Basel.

Timar-Geng Z., Fügenschuh B., Wetzel A., Dresmann H., 2006. Low-temperature thermochronology of the flanks of the southern Upper Rhine Graben. International Journal of Earth Sciences 95, 685–702. https://doi.org/10.1007/s00531-005-0059-1

Turab S.A., Stüwe K., Stuart F.M., Cogne N., Chew D.M., Robl J., 2023. A two phase escarpment evolution of the Red Sea margin of southwestern Saudi Arabia. Insights from low-temperature apatite thermochronology. Earth and Planetary Science Letters 603, 117990. https://doi.org/10.1016/j.epsl.2023.117990

v. Gessel S., Hintersberger E., v. Ede R., ten Veen J., Doornenbal H., Diepolder G.W., den Dulk M., Hamiti S., Vukzaj N., Çako R., Prendi E., Ceroni M., Mara A., Barros R., Tovar A., Britze P., Baudin T., Stück H., Jähne-Klingberg F., Jahnke C., Höding T., Malz A., Kristjánsdóttir S., Þorbergsson A., Di Manna P., D'Ambrogi C., Congi M., Lazauskien J., Andriuškevičien G., Baliukevičius A., Jarosiński M., Gogolek T., Stępień U., Krzemińska E., Salwa S., Habryn R., Aleksandrowski P., Szynkaruk E., Konieczyńska M., Ressurreição, R., Machado S., Moniz C., Sampaio J., Dias R., Carvalho J., Fernandes J., Ramalho E., Filipe A., Celarc B., Atanackov J., Jamšek Rupnik P., Shevchenko A., Melnyk I., Lapshyna A., 2021. The HIKE European Fault Database (EFDB) compiled in the framework of the GeoERA project HIKE (2018–2021).

Weissel J.K., Karner G.D., 1989. Flexural uplift of rift flanks due to mechanical unloading of the lithosphere during extension. Journal of Geophysical Research 13919–13950.

Wetzel A., Allenbach R., Allia V., 2003. Reactivated basement structures affecting the sedimentary facies in a tectonically "quiescent" epicontinental basin: an example from NW Switzerland. Sedimentary Geology 157, 153–172. https://doi.org/10.1016/S0037-0738(02)00230-0

Wildman M., Cogné N., Beucher R., 2019. Fission-Track Thermochronology Applied to the Evolution of Passive Continental Margins, in: Malusà, M.G., Fitzgerald, P.G. (Eds.), Fission-Track Thermochronology and Its Application to Geology, Springer Textbooks in Earth Sciences, Geography and Environment. Springer International Publishing, Cham, 351–371.

Wilson M., Rosenbaum J.M., Dunworth E.A., 1995. Melilitites: partial melts of the thermal boundary layer? Contr. Mineral. and Petrol. 119, 181–196. https://doi.org/10.1007/BF00307280

Wolff R., Dunkl I., Lange J.-M., Tonk C., Voigt T., von Eynatten H., 2015. Superposition of burial and hydrothermal events: post-Variscan thermal evolution of the Erzgebirge, Germany. Terra Nova 27, 292–299. https://doi.org/10.1111/ter.12159

Wu L., Shi G., Danišík M., Zhang Z., Wang Y., Wang F., 2019. MK -1 Apatite: A New Potential Reference Material for (U-Th)/He Dating. Geostandards and Geoanalytical Research 43, 301–315. https://doi.org/10.1111/ggr.12258

Wu L., Wang F., Zhang Z., Shi G., Danišík M., He D., Sun J., Wang Y., Shen X., Zaw T., 2021. Reappraisal of the applicability of MK-1 apatite as a reference standard for (U Th)/He geochronology. Chemical Geology 575, 120255. https://doi.org/10.1016/j.chemgeo.2021.120255

Zeh A., Zimmermann M., Albert R., Drüppel K., Gerdes A., 2024. Zircon

U-Pb-Hf isotope systematics of southern Black Forest gneiss units (Germany) – Implications for the pre-Variscan evolution of Central Europe. Gondwana Research 128, 351–367. https://doi.org/10.1016/j.gr.2023.11.008

Ziegler P.A., 1992. European Cenozoic rift system. Tectonophysics 208, 91–111. https://doi.org/10.1016/0040-1951(92)90338-7

Ziegler P.A., 1990. Geological Atlas of Western and Central Europe, (2nd and completely rev.). ed. Geological Society Pub. House.

Ziegler P.A., Cloetingh S., Van Wees J.-D., 1995. Dynamics of intra-plate compressional deformation: the Alpine foreland and other examples. Tectonophysics 252, 7–59. https://doi.org/10.1016/0040-1951(95)00102-6

Ziegler P.A., Dèzes P., 2007. Cenozoic uplift of Variscan Massifs in the Alpine foreland: Timing and controlling mechanisms. Global and Planetary Change 237–269. https://doi.org/10.1016/j.gloplacha.2006.12.004

Ziegler P.A., Schumacher M.E., Dèzes P., van Wees J.-D., Cloetingh S., 2004. Post-Variscan evolution of the lithosphere in the Rhine Graben area: constraints from subsidence modelling. Geological Society, London, Special Publications 223, 289–317. https://doi.org/10.1144/GSL.SP.2004.223.01.13

Received: 9.11.2025
Accepted: 5.2.2026
Editorial Handling: Kurt Stüwe